TARGETED DEEP BRAIN STIMULATION OF THE MOTOR THALAMUS FACILITATES VOLUNTARY MOTOR CONTROL AFTER CORTICO-SPINAL TRACT LESIONS

Jonathan C. Ho[1,2,*], Erinn M. Grigsby[2,3,*], Arianna Damiani[2,4,5], Lucy Liang[2,4,5], Josep-Maria Balaguer[2,4,5], Sridula Kallakuri[2,7,8], Jessica Barrios-Martinez[6], Vahagn Karapetyan[2,4,5], Daryl Fields[2,6], Peter C. Gerszten[6], T. Kevin Hitchens[8], Theodora Constantine[6], Gregory M. Adams[6], Donald Crammond[6], Marco Capogrosso[2,4,5,6], Jorge A. Gonzalez-Martinez[6**], Elvira Pirondini[2,3,4,5,6,8**]

1. School of Medicine, University of Pittsburgh, Pittsburgh, PA, USA
2. Rehab and Neural Engineering Labs, University of Pittsburgh, Pittsburgh, PA, USA
3. Department of Physical Medicine and Rehabilitation, University of Pittsburgh, Pittsburgh, PA, USA
4. Department of Bioengineering, University of Pittsburgh, Pittsburgh, PA, USA
5. Center for the Neural Basis of Cognition, Pittsburgh, PA, USA
6. Department of Neurological Surgery, University of Pittsburgh, Pittsburgh, PA, USA
7. Department of Neuroscience, University of Pittsburgh, Pittsburgh, PA, USA
8. Department of Neurobiology, University of Pittsburgh, Pittsburgh, PA, USA

(*) Co-first author
(**) Co-last author

Cerebral white matter tract lesions prevent cortico-spinal descending inputs from effectively activating spinal motoneurons, leading to untreatable muscle paralysis. However, in most cases the damage to cortico-spinal axons is incomplete and the spared connections could be potentiated by neurotechnologies to restore motor function. Here we hypothesized that, by engaging direct excitatory connections to cortico-spinal motoneurons, deep brain stimulation (DBS) of the motor thalamus could facilitate activation of spared cortico-spinal fibers improving movements of the paretic limb. We first identified, in monkeys, optimal stimulation targets and parameters that enhanced motor evoked potentials to arm, hand, and face muscles, as well as grip forces. This potentiation persisted after cerebral white matter lesions. We then translated these results to human subjects by identifying the corresponding optimal thalamic targets (VIM/VOP nuclei) and replicated the results obtained in monkeys. Finally, we designed a DBS protocol that immediately improved voluntary grip force control in a patient with a chronic traumatic brain injury. Our results suggest that targeted DBS of the motor thalamus may become an effective therapy for motor paralysis.

INTRODUCTION

Lesions of the cortico-spinal tract (CST), as a consequence of stroke or traumatic brain injury (TBI), disrupt communication between the cortex and lower motor centers leading to a loss of function in face, upper or lower limb muscles[1–4]. Consequent upper-limb motor deficits significantly affect the quality of life of approximately 10 million people only in the United States[5,6]. Intense physical therapy remains the only routine intervention, but with limited efficacy, in particular for patients with moderate to severe paresis[7,8].

In most cases, damage to the CST is incomplete. Yet the spared excitatory descending connections are insufficient to activate the spinal motoneurons, leading to functional motor paresis[9–11]. Facilitation of the activation of the residual cortico-spinal axons could reestablish the

missing excitation restoring voluntary muscle control. This facilitation could be achieved by a technology capable of modulating the excitability of cortico-spinal neurons in the motor cortex, thereby increasing CST output and, as a consequence, enhancing movements of the paretic limb[12,13].

We conjectured that deep brain stimulation (DBS) could be a viable approach to modulate the excitability of cortico-spinal neurons. Indeed, DBS is a clinically approved highly focal intervention that entails the implantation of stimulating electrodes within subcortical regions[14,15]. While certain DBS mechanisms of action are still unclear, we know that stimulation-induced action potentials within the subcortical targets propagate through axon terminals to recipient cortical areas modulating their neural activity[16–18]. Therefore, DBS can be programmed to affect restricted cortical areas by targeting subcortical brain regions that preferentially project axons to those areas.

For instance, previous studies have demonstrated that DBS of thalamic and subthalamic nuclei affect motor cortex excitability. Specifically, motor evoked potentials (MEPs) elicited by transcranial magnetic stimulation (TMS) were modulated when conditioned by DBS of subcortical brain areas with direct (ventral thalamus) and indirect (globus pallidus pars interna, GPi and subthalamic nucleus, STN) projections to the motor cortex[16,18–21].

Based on these results and the known anatomical evidence of direct connections to the motor cortex from the motor thalamic nuclei[20,22–25], we hypothesized that DBS of the motor thalamus could be tailored to improve motor paresis after lesions of the CST. However, optimization of DBS for treating paralysis requires identifying which nuclei of the motor thalamus should be targeted and which stimulation parameters would maximize both therapy specificity and efficacy.

Here, we overcame these scientific and technological challenges with a translational experimental framework that leveraged experiments in monkeys, i.e., the most relevant animal model for CST anatomy and function[26–28], to identify possible mechanisms of action, and subsequently validated these findings in human patients. Specifically, we 1) identified the nucleus of the motor-sensory thalamus with dense, direct, and preferential excitatory connections to cortico-spinal neurons in primary motor cortex; 2) designed a series of electrophysiology experiments in monkeys and human patients to test whether DBS of this nucleus could augment excitability of the motor cortex with high specificity to cause increased motor output; and 3) optimized DBS parameters for maximal therapeutic effects. We then built on these findings to demonstrate that targeted DBS of the motor-sensory thalamus increased muscle activation, strength, and force control after lesions of the CST in intraoperative monkeys and human experiments. Finally, we verified that these effects lead to improved functional performance during behavioral tasks in a subject with chronic TBI and a DBS system implanted in the motor thalamus.

Overall, our results demonstrated the feasibility of targeted and optimized DBS for upper-limb paresis, paving the way towards a novel effective therapy for motor deficits after CST lesions.

RESULTS

Thalamocortical projections from the monkey motor-sensory thalamus

Since we aimed at increasing the excitability of cortico-spinal neurons within the primary motor cortex, we sought to identify the optimal stimulation target by localizing a subcortical region that has a high number of direct excitatory projections to the motor cortex and that could be targeted by existing DBS clinical leads and neurosurgical implant strategy. Based on previous anatomical evidence, we posited that the motor-sensory (or motor) thalamus could be this optimal target[20,22,24,29]. In humans, the motor thalamus includes four nuclei that have different preferential projection targets: the ventral anterior (VA), the ventral oral posterior (VOP), the ventral intermediate (VIM), and the ventral caudal nucleus (VC)[30,31]. Thalamocortical fibers originating in the VC project preferentially to the somatosensory cortex, whereas those originating in the VIM/VOP connect to the motor cortex, and those in the VA to the pre-motor cortex. We first acquired and analyzed high-resolution diffusion magnetic resonance imaging (MRI) data using high-definition fiber tracking (HDFT) in monkeys (n=3) to confirm whether the monkey motor thalamus had a similar anatomical organization. We focused our analysis on the three nuclei of the monkey motor thalamus: the ventral anterolateral (VAL), the ventral laterolateral (VLL), and the ventral posterolateral (VPL) nuclei[23–25,32–34]. We reconstructed all the likely axonal pathways between these nuclei and the somatosensory, motor, and premotor cortical areas and quantified the relative strength of these connections by calculating the volume of thalamocortical projections from each nucleus to each cortical region normalized by the total volume of fibers (**Figure 1a**). We confirmed a clear functional and somatotopic organization of the thalamic nuclei that parallel the organization of the human thalamocortical connections, with axonal projections preferentially towards the somatosensory cortex from the posterior motor thalamus (VPL) and preferentially towards motor and pre-motor cortices from the anterior motor thalamus (i.e., VLL and VAL). Using selectivity detection analysis among the three nuclei, we found that the VLL nucleus, which corresponds to the human VIM/VOP nucleus, had the greatest selectivity of the projections towards M1 (VPL: 0.67, VLL: 0.89, VAL: 0.33). We, therefore, considered it the optimal target for our DBS strategy.

A robotic stereotactic approach to the motor thalamus in monkeys

To enable a highly precise implantation of the stimulating electrodes in the VLL in monkeys, we repurposed a medical-grade MRI-guided robotic stereotactic device (**Figure 1b**). This allowed us to design implantation procedures similar to those that could be surgically applied in humans thus facilitating immediate translation of our results to patients. We used the ROSA ONE® Robot Assistance Platform (ROSA robot, Zimmer Biomet, Warsaw, Indiana, USA) to place a human-grade electrode (Microdeep® SEEG Electrodes, DIXI Medical, Marchaux-Chaudefontaine, France) within the VLL nucleus in anesthetized monkeys (n=5) (**Extended Figure 1**). High-definition anatomical MRIs were obtained to plan a single trajectory to the VLL that avoided the sensory and motor cortices. MRIs were then fused to computer tomography (CT) scans obtained after implantation of five fiducial titanium skull screws to use as reference points for co-registration of the robot during surgery. Co-registration errors were small (MK-SC: 0.39 mm, MK-SZ: 0.32 mm, MK-OP: 0.25 mm, MK-HS = 0.29 mm, MK-JC = 0.33 mm), thus ensuring highly precise implantation[35]. These errors were consistent with our previous report[36] **(Extended Data Figure 1**) and similar to the errors observed in human DBS implantations (0.27 ± 0.07 mm)[37]. At the end

of the experimental procedures, we created a small thermocoagulation lesion at the electrode tip to allow post-mortem visualization of the implant location. High-resolution post-mortem structural MRI confirmed the accurate location of the DBS electrode within the VLL (**Figure 1c**). Additionally, we used HDFT between the electrode implantation region and the somatosensory, motor, and pre-motor cortical areas and confirmed that the largest volume of fibers within the stimulation field projected to M1 (on average 55% of the fibers) (**Figure 1c**).

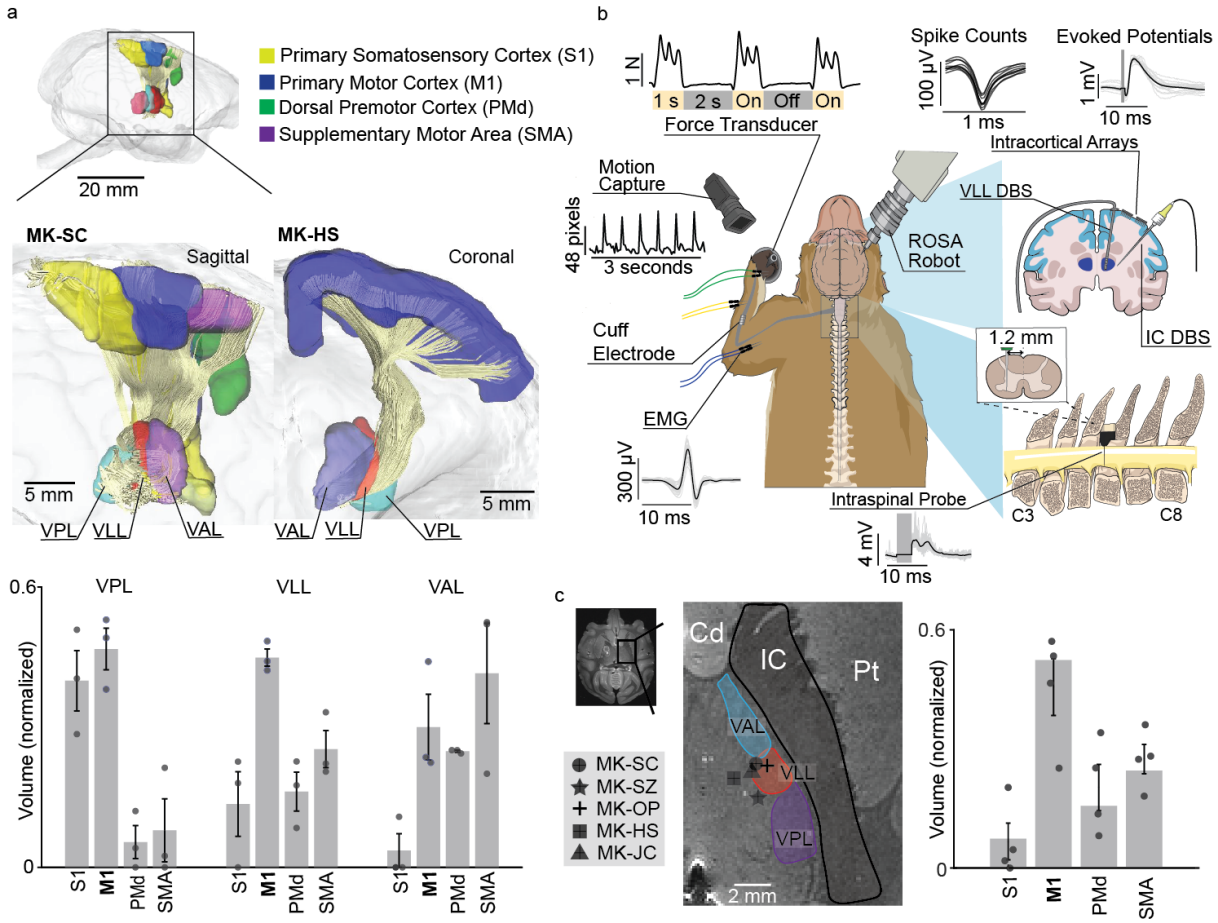

Figure 1: Characterization of monkey thalamocortical projections.
(a) *Top:* High definition fiber tracking (HDFT) from VPL, VLL, and VAL nuclei (VPL: ventral posterolateral, VLL: ventral laterolateral, VAL: ventral anterolateral) of monkey motor-sensory thalamus to cortical regions (n=3) (S1: primary somatosensory cortex, M1: primary motor cortex, PMd: dorsal pre-motor cortex, SMA: supplementary motor area). *Bottom:* Normalized volume of thalamocortical projections (mean ± standard error) from each nucleus to each cortical region normalized by the total volume of fibers. **(b)** Acute experimental setup. First, a cuff electrode was implanted around the motor branch of the radial nerve for stimulation. Animals were then implanted with a DBS electrode in the internal capsule (IC) and one in the VLL using the ROSA robot and intracortical arrays over S1 and M1. An intraspinal probe was implanted at the C6 spinal segment to record spinal local field potentials and EMG needle electrodes were inserted in arm, hand, and face muscles. A force transducer was placed in the animal's hand to measure grip force. Finally, a camera recorded the kinematics of the arm and hand. **(c)** *Left:* VLL Electrode implant location for each animal. Implant locations were localized from post-mortem MRI where the thermo-ablation lesion was

visible (Cd: Caudate Nucleus, IC: Internal Capsule, Pt: Putamen). *Right:* Normalized volume HDFT projections from the area of stimulation to cortical regions (n=4).

Targeted deep brain stimulation of the VLL specifically excites the motor cortex

Previous studies have revealed that the thalamocortical projections, as identified with our HDFT analysis, are glutamatergic[22,38]. We therefore hypothesized that stimulation of the VLL would excite the motor cortex. To demonstrate this hypothesis, in addition to the DBS electrode within the VLL nucleus, we implanted two 48-channels intracortical arrays (Utah arrays) in the primary motor and somatosensory cortices, respectively (**Figure 1b**). In n=4 anesthetized monkeys, we applied continuous stimulation of the VLL at 10 Hz (see **Supplementary Table 2** for details on stimulation parameters) while recording local field potentials and multi-unit neuronal activity from these cortical areas (**Figure 2a**). We then analyzed VLL stimulation triggered averages of evoked potentials in M1 and S1 electrodes and observed clear cortical evoked potentials with peak latencies at 5-10 ms post-stimulation (see example **Figure 2b**) confirming a direct monosynaptic pathway between the VLL and cortex[39,40]. Analysis of peak to peak amplitude across the entire arrays showed significantly larger responses in M1 as compared to S1 in all monkeys (see histograms **Figure 2b**), confirming preferential projections of VLL axons towards M1. Interestingly, these responses were larger along the pre-central gyrus where the hand and arm representation in M1 are located (see heat maps **Figure 2b**). Stimulation-evoked spike counts corroborated these findings showing an increase in multi- and single-units firing rates post-stimulation (**Figure 2c**). As expected, this increase was significantly stronger in M1 as compared to S1.

Cortical evoked potentials elicited from VLL stimulation should be indicative of increased excitability of cortico-spinal neurons. If this is true, the amplitude of antidromic neural responses elicited in cortical-spinal axons from stimulation of the CST and recorded in M1 should be larger when VLL stimulation is active. To test this property, a stimulating electrode was implanted into the posterior limb of the internal capsule (IC) (**Figure 1b**), which contains the cortical-spinal axons originating in the motor cortex and projecting to the spinal cord. We targeted the hand representation of the CST. Direct stimulation of these axons creates both orthodromic action potentials towards the spinal motoneurons (**Figure 5c**) and antidromic action potentials toward the cell body of the pyramidal neurons in M1, which could be recorded through the intracortical electrodes (**Figure 2d**). We confirmed implantation within the CST passing through the IC observing MEPs of upper arm and hand muscles (10-15 ms post-stimulation, **Figure 3b**) and antidromic evoked potentials in M1 at shorter latencies (5ms post-stimulation, **Figure 2d**). We then delivered single pulse stimulation to the IC conditioned by a 100ms burst at 100 Hz to the VLL nucleus at different delays (2-50ms). We found that the peak to peak amplitude of the antidromic neural responses in M1 was significantly higher when a burst of VLL stimulation conditioned IC stimulation (n=3) (**Figure 2d**) confirming that VLL stimulation increases excitability of cortico-spinal neurons. At delays higher than 10ms, the antidromic potentials returned to amplitudes similar to those of IC stimulation alone.

Overall, these results demonstrate that DBS of the VLL nucleus increases the excitability of cortico-spinal neurons specifically within M1.

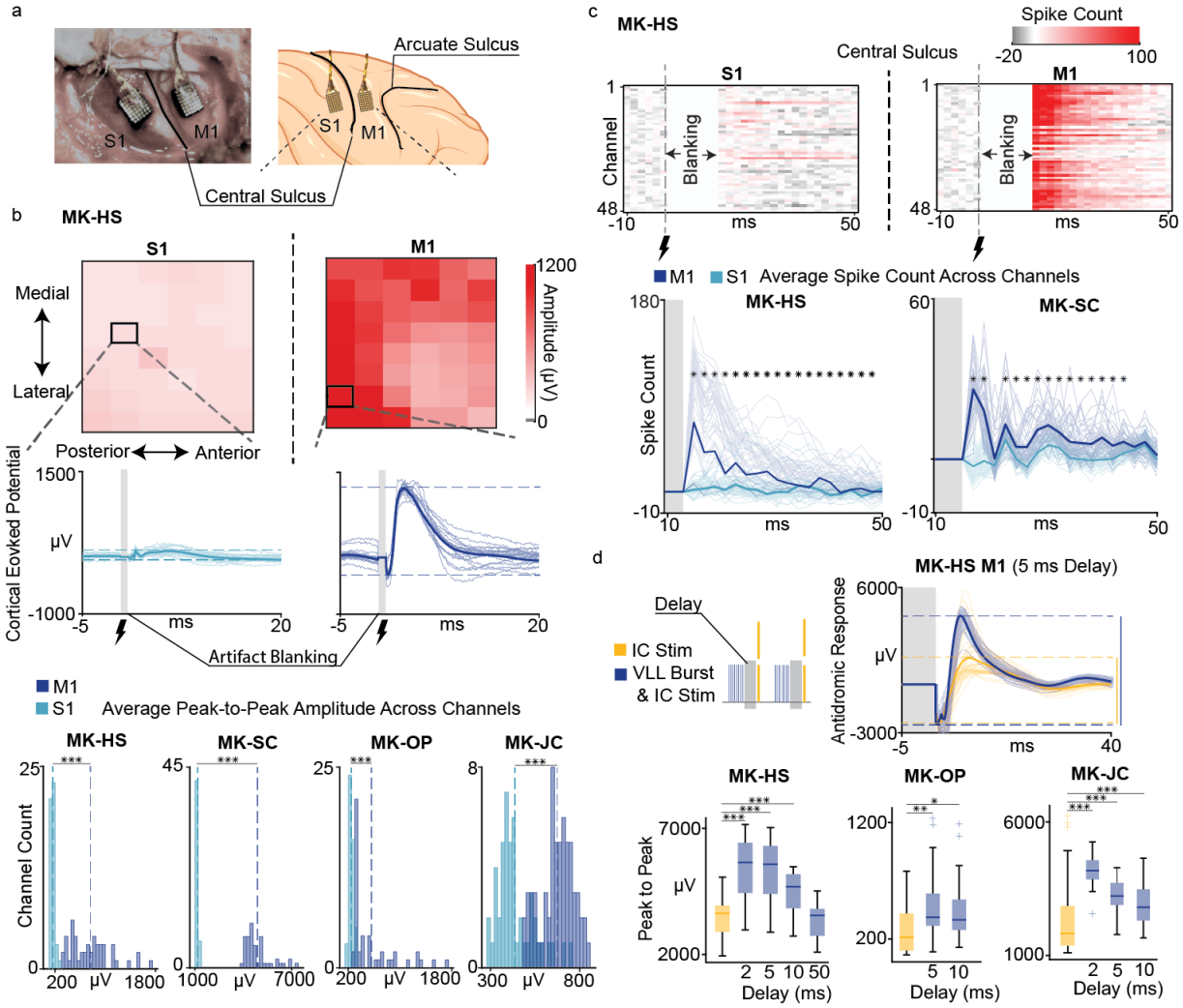

Figure 2: DBS increases motor cortex excitability.
(a) Implant location of M1 and S1 intracortical arrays. **(b)** *Top:* Example heatmap of average peak to peak amplitudes of cortical evoked potentials from VLL stimulation at 10 Hz across all channels over S1 and M1 for one animal. *Center:* Example stimulation triggered averages of cortical evoked potentials over S1 and M1 (n=40 traces) for one animal. *Bottom:* Histogram of peak to peak amplitudes across all channels for S1 and M1 (n=48 channels per array). **(c)** *Top:* Example baseline corrected spike count heatmaps in S1 and M1 for one animal. *Bottom:* Average spike counts over time across all channels in S1 and M1 array (n=48 channels per array). **(d)** *Top:* Example traces of antidromic potentials in M1 from IC stimulation without (yellow) and with (blue) conditioning from a burst of VLL stimulation for one animal (n=40 traces). Boxplot of peak to peak amplitude of the antidromic potentials when IC stimulation is conditioned by VLL stimulation at various delays (2, 5, 10, and 50ms). For all panels, statistical significance was assessed with one-tail bootstrapping with Bonferroni correction: $p<0.05$ (*), $p<0.01$ (**), $p<0.001$(***).

Motor thalamus stimulation potentiates upper-limb motor outputs

We built on previous experiments that reported modulated MEPs from TMS of the motor cortex when conditioned with DBS of VIM, GPi, or STN[16,19–21], and we hypothesized that the enhanced

cortical excitability observed in our monkeys would lead to amplified MEPs recorded in arm, hand, and face muscles. Specifically, we paired stimulation of the IC at 2 Hz with continuous stimulation of VLL at 50 Hz or 100 Hz (**Figure 3a**). Stimulation of the IC at 2 Hz generated MEP responses in hand, arm, and face muscles as well as movements of the arm and face (**Figure 3b**) at short latencies (on average 10-15 ms) suggesting a monosynaptic activation of motoneurons. When 2 Hz IC stimulation was paired with continuous stimulation of the VLL at 50 Hz and 100 Hz, peak to peak amplitude of both MEPs and movements of the arm (n=2) and hand (n=3) were immediately and significantly increased (**Figure 3b**, **Extended Data Figure 2** and **3**). Interestingly, MEP peak to peak amplitudes increased proportionally to VLL stimulation amplitude (**Figure 3a**). In one animal, VLL stimulation also increased face muscles MEPs (**Figure 3d**). While the frequency at which maximal increases were obtained varied across animals and muscles (50 Hz or 100 Hz), MEPs and movement were augmented in all tested monkeys (**Extended Data Figure 2** and **3**). More specifically, VLL stimulation at 50 Hz most often increased MEP amplitudes in the upper-limb and face; whereas, stimulation at 100 Hz would produce either greater amplification or in some instances a suppression of MEPs (**Figure 3b**, **Figure 5a**).

Finally, in order to demonstrate that VLL stimulation could enhance induced functional movements, we delivered bursts of IC stimulation at about 50 Hz which induced a grasping motion producing measurable isometric forces (**Figure 3c**). We then paired the functional IC stimulation with VLL stimulation at 50 Hz or 100 Hz. VLL stimulation at 50 Hz, but not at 100 Hz, immediately and significantly increased the grip force as compared to no VLL stimulation (n=1) (**Figure 3c**).

In summary, direct motor thalamus stimulation increased upper-limb motor output as measured by the amplitude of arm and hand muscle MEPs and movement kinematics, and stimulation-induced grip forces.

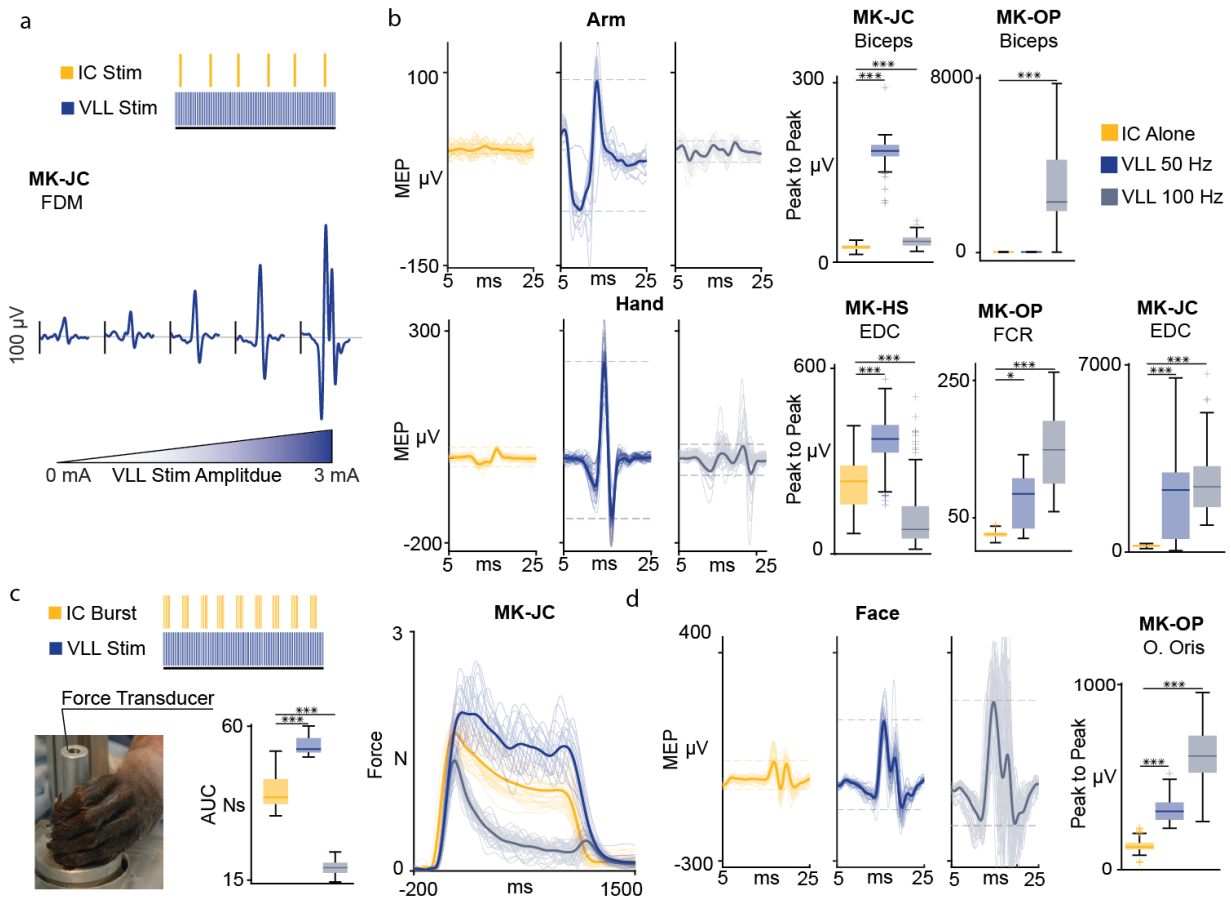

Figure 3: DBS amplifies motor outputs.

(a) Example of Flexor Digitorum Minimi (FDM) motor evoked potentials (MEPs) generated by IC stimulation at 2 Hz paired with continuous VLL stimulation with gradual ramp up of amplitude (0 to 3mA). **(b)** MEPs of one arm muscle (n=40, Biceps, Mk-JC) and one hand muscle (n=40, EDC, Mk-HS) with IC stim alone and then paired with VLL stim at 50 Hz and 100 Hz. Boxplots of the peak to peak amplitudes of the MEPs (Biceps, FCR: Flexor Carpi Radialis, EDC: Extensor Digitorum Communis). **(c)** Force transducer experimental setup and stimulation parameters (IC 45-50 Hz burst, 1s on, 2s off; VLL 50 Hz continuous). Example force traces (n=20) and boxplots of area under the curve (IC alone, IC with VLL at 50 Hz, and IC with VLL at 100 Hz). **(d)** MEPs of one face muscle (n=40, Orbicularis Oris, Mk-OP) with IC stim alone and then paired with VLL stim at 50 Hz and 100 Hz and boxplots of peak to peak amplitudes. For all panels, statistical significance was assessed with one-tail bootstrapping with Bonferroni correction: $p<0.05$ (*), $p<0.01$ (**), $p<0.001$(***).

Control experiments: motor output potentiation occurs through orthodromic thalamocortical pathways

We sought to confirm that the enhanced motor outputs were the result of an increased excitability of the motor cortex and did not result instead from inadvertent activation of descending excitatory tracts from current spread. We reasoned that if the observed MEP potentiation was occurring within the spinal cord as a result of inadvertent descending action potentials in other excitatory tracts, then we would expect that peripheral inputs to spinal circuits, such as H-reflexes, would also be modulated by VLL stimulation. To control for this, we implanted a multi-channel linear

probe (NeuroNexus) at the C6-C7 spinal level with dorsal-ventral orientation (**Figure 1b**). We observed consistent volleys in the spinal cord in the first 3 ms following VLL stimulation (1.44 ms, 1.73, and 2.13 ms for Mk-OP, Mk-JC, and Mk-HS, **Figure 4a**) with largest peak to peak amplitude in the intermediate-ventral spinal cord gray zone (**Figure 4b**). These evoked potentials could either represent antidromic recruitment of ascending pathways such as spino-thalamic axons, or orthodromic activation of descending excitatory pathways. However, there were no MEPs in either the upper-limb or facial muscles when stimulating the VLL nucleus alone (**Figure 4c**, **Extended Data Figure 4**) suggesting that the observed spinal responses were not caused by inadvertent stimulation of the CST. Moreover, the frequency of the movements when we simultaneously stimulated the VLL and the IC was at 2 Hz (i.e., same frequency of IC stimulation) and not at the frequencies of VLL stimulation (50 or 100 Hz) (**Extended Data Figure 3**), further demonstrating that the increase in MEPs and movement kinematic was not induced by current spread from VLL to the CST. It was still possible that the observed spinal responses and the enhanced movements could be carried by other descending tracts that do not have direct spinal motor neuron connections or generate MEPs but that are able to excite the spinal circuits and facilitate movement. However, when we paired continuous VLL stimulation at 50 Hz with stimulation of the radial nerve we observed no significant increase of reflex-mediated responses (**Figure 4d** and **Extended Data Figure 5**). These results demonstrate that 1) the observed volleys in the spine are likely the result of antidromic activation of ascending pathways such as spino-thalamic axons; and 2) the observed potentiation of MEPs (**Figure 3**) is not occurring inside the spinal cord as a result of current spread to descending axons, but is, instead, a trans-cortically mediated effect.

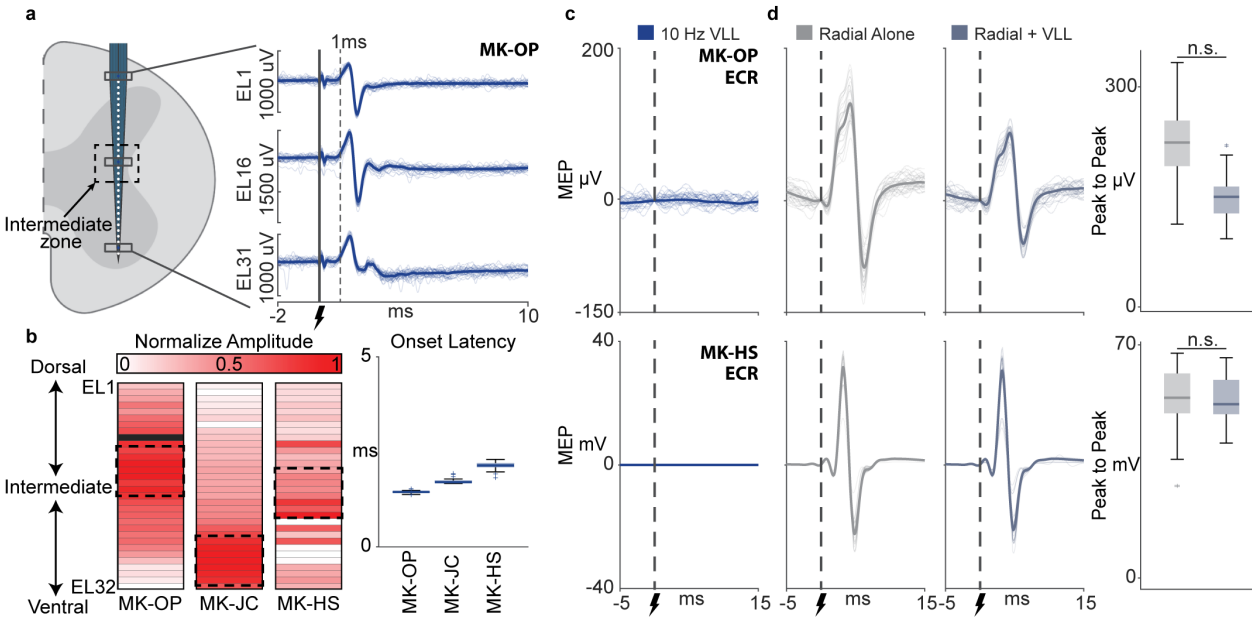

Figure 4: Motor output potentiation is not through spinal circuits.

(a) Example of antidromic responses in the spinal cord from VLL stimulation at 10 Hz (n=30 traces) in one monkey. **(b)** *Left:* Heatmaps of peak to peak amplitude of the antidromic responses in the spinal cord at the C6-C7 spinal level with dorsal-ventral alignments for n=3 animals. The dashed boxes are highlighting the putative intermediate-ventral zone where we see the greatest responses. *Right:* Boxplots of the antidromic response latency for each animal (n = 656 MK-OP, n = 596 MK-JC, n = 289 MK-HS). **(c)** MEPs of the wrist (ECR: Extensor Carpi Radialis, 30 traces for each animal) elicited by VLL stim at 10 Hz. **(d)**

EMG reflexes of the ECR muscle elicited by radial nerve stimulation and radial nerve paired with continuous VLL stimulation at 50 Hz (30 example traces each). Boxplots of the peak to peak amplitudes of the EMG reflexes elicited by radial nerve stimulation alone and radial nerve stimulation paired with continuous VLL stimulation at 50 Hz. For all panels, statistical significance was assessed with one-tail bootstrapping with Bonferroni correction, however, in all cases the results were not significant.

Efficacy of VLL stimulation in promoting motor augmentation is frequency dependent

Our results suggest that the potentiation of descending CST activity is mediated by the orthodromic recruitment of cortico-spinal neurons in M1 via thalamocortical excitatory synaptic projections. Excitatory synaptic transmission is known to be affected by stimulation frequency via mechanisms such as presynaptic inhibition or homosynaptic neurotransmitter suppression[41]. Accordingly, we explored the effect of multiple frequencies on the efficacy of motor potentiation. We delivered IC stimulation at 2 Hz paired with continuous VLL stimulation at 10, 50, 80, 100, and 200 Hz. We analyzed the MEP responses to the individual IC stimulation pulses over time and observed a variety of modulation patterns. (**Figure 5a**). We classified these patterns to five distinct categories: (1) *no potentiation,* as responses were comparable to IC stimulation alone, (2) *initial adaptation*, as responses were amplified upon activation of VLL stimulation but only after an initial transient period of 5–20 responses, (3) *potentiation,* as responses were potentiated, (4) *attenuation*, as the response amplitudes progressively decreased compared to the initial responses, and (5) *suppression*, as the responses were completely suppressed after a few pulses. Generally, the absence of potentiation of the IC stimulation responses was characteristic of low frequencies (10 Hz), whereas stimulation frequencies between 50 Hz and 80 Hz consistently increased the MEP amplitudes with sustained outputs (**Figure 5b**). Stimulation at 100 Hz, instead, resulted in *potentiation* and *initial adaptation* of responses, but effects varied across muscles with some instances of MEP *suppression*. Finally, *attenuation* and *suppression* of responses were more likely to happen at higher frequencies and particularly at 200 Hz. Therefore, we identified the 50-100 Hz range as optimal to achieve sustained potentiation of MEPs.

We further explored the neural correlates of these effects with intra-cortical and intra-spinal neural recordings. Consistent with the EMG recordings, intra-spinal neural responses elicited by IC stimulation pulses in the ventral zone[42], where spinal motoneurons are located, had significantly larger peak to peak amplitudes when the VLL nucleus was stimulated at 50 or 80 Hz (**Figure 5c**). Spinal responses were, instead, suppressed at higher frequencies. Similarly, cortical evoked potentials in M1 when stimulating the VLL alone showed stronger peak to peak amplitudes with frequencies of stimulation in the 50-80 Hz range as compared to 100 Hz (**Figure 5d**). These combined results demonstrate that the effects observed in the MEP and spinal cord responses were a consequence of frequency dependent excitation of the motor cortex. This frequency dependent characteristic of excitation could be either the result of presynaptic inhibition or homosynaptic neurotransmitter suppression at the level of the cortico-spinal neurons[29,41,43].

In summary, our analysis confirmed a frequency dependent effect that is consistent with motor cortical potentiation of thalamic afferents to M1 cortex via excitatory synaptic inputs. From these findings, we identified that the optimal stimulation frequencies to increase muscle outputs are in the 50-100 Hz range, notably lower than clinical DBS stimulation frequencies (~130 Hz)[44].

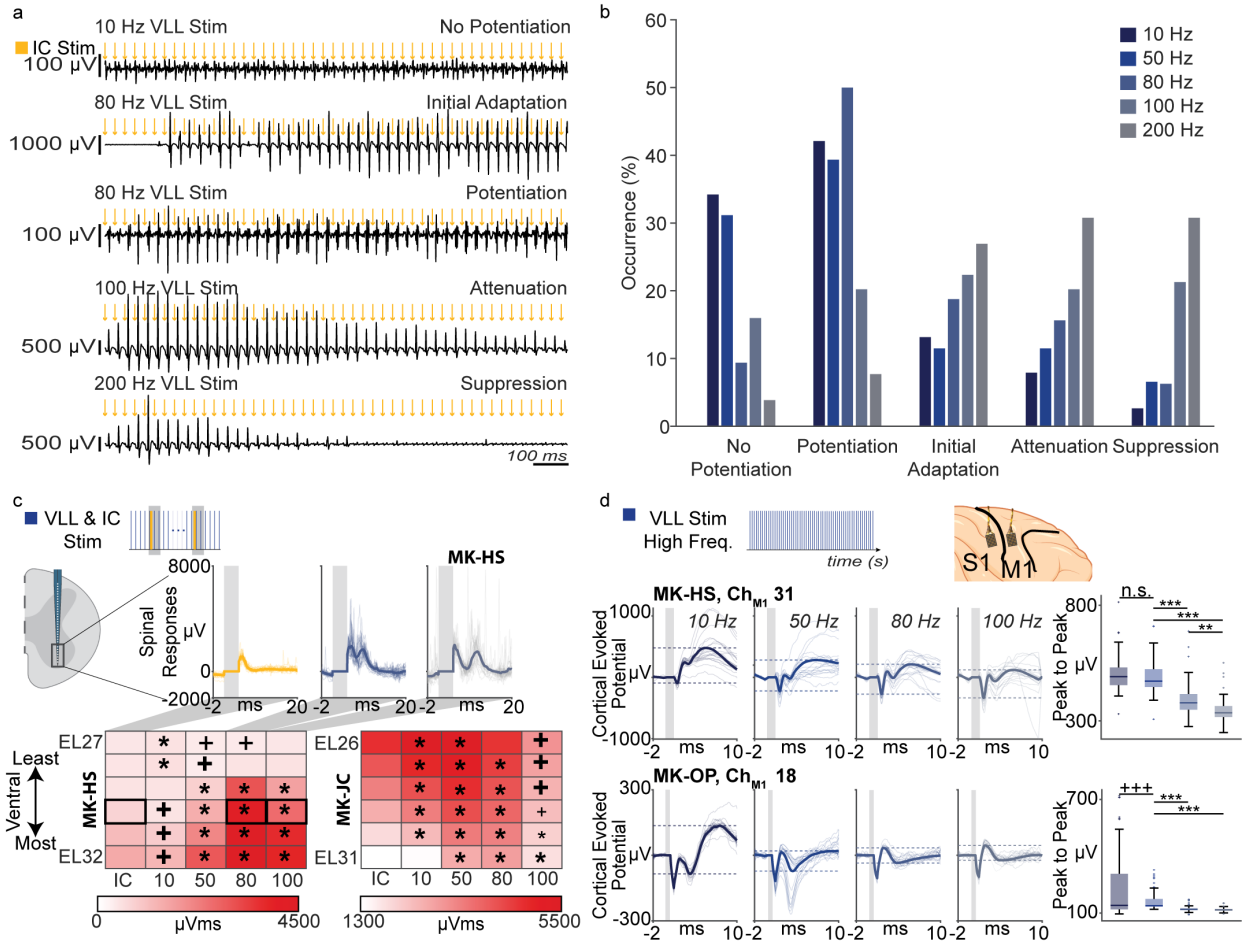

Figure 5: Responses are modulated in a frequency-dependent manner.
(a) Examples of frequency-dependent modulation of muscular responses. EMG responses were elicited by 2 Hz stimulation of the IC paired with different VLL stimulation frequencies (10, 50, 80, 100, and 200 Hz). The stimulation amplitude for both IC and VLL were held constant for all conditions. **(b)** The occurrence frequency of modulation patterns with respect to stimulation frequency. All patterns recorded in all muscles of 3 animals in which high-frequency stimulation was tested were included in the analysis (n= 35 patterns at 10 Hz, n=56 patterns at 50 Hz, n=30 patterns at 80 Hz, n=90 at 100 Hz, and n=21 patterns at 200 Hz). **(c)** *Top:* Example of spinal responses in the ventral zone for IC stimulation alone and IC stimulation paired with VLL stimulation at 80 and 100 Hz (n = 30 traces per plot). *Bottom:* Heatmaps of the average area under the curve (AUC) calculated from 5 to 10 ms after IC stimulation for all ventral channels for IC stimulation alone (n = 77 MK-HS, n = 37 MK-JC) and IC stimulation paired with VLL stimulation at 10 (n = 227 MK-HS, n = 113 MK-JC), 50 (n = 222 MK-HS, n = 90 MK-JC), 80 (n = 233 MK-HS, n = 90 MK-JC), and 100 Hz (n = 234 MK-HS, n = 90 MK-JC). (*) for significant potentiation and (+) for significant suppression. Bold represents p<0.001. **(d)** *Top:* Schematic of the experimental layout for testing frequency dependence within the motor cortex. *Bottom:* Example traces of the cortical evoked potential responses in the M1 array when stimulating the thalamus at different frequencies (10, 50, 80, and 100 Hz) (n = 30 traces). Dashed lines show the average bound of the peak to peak values. Boxplots of the peak to peak amplitudes of the cortical evoked potentials. Statistical significance was tested by comparing 50 Hz VLL stimulation to all other stimulation conditions for potentiation using one-tailed bootstrapping with Bonferroni correction: p<0.05 (*), p<0.01 (**), p<0.001(***).

Potentiation of motor outputs persists after CST lesions

To demonstrate the potential clinical relevance of our approach, we verified whether electrical stimulation of the VLL nucleus would still augment motor outputs after a lesion of the CST. A partial lesion of the IC would reduce the number of CST fibers projecting to the cervical spinal cord, leading to motor deficits similar to those observed in stroke and TBI patients. To create such a lesion, we implanted a second depth electrode in the posterior limb of the IC, approximately 2 cm ventral from the IC stimulating electrode. We then generated a controlled and reproducible lesion of the CST fibers by performing thermo-frequency ablations[45] through the ventral electrode (**Figure 6a**). As expected, we observed reduced MEP amplitudes when stimulating the dorsal IC electrode after the ventral lesion had been made (**Figure 6b** and **6c**). Post-mortem HDFT confirmed that the lesion consistently and significantly reduced the volume of CST fibers compared to the intact hemisphere in all tested monkeys (70% of reduction) (n=4) (**Figure 6a**). After the IC lesion, the smaller MEPs recorded from the arm, hand and face muscles were significantly increased when the VLL nucleus was simultaneously stimulated at 50 and 100 Hz (**Figure 6b** and **6c, Extended Data Figure 6** and **Extended Data Figure 7**). MEP amplitudes when VLL stimulation was ON were comparable to pre-lesional MEP amplitudes in the same muscles. Importantly, also the grip force elicited by IC stimulation bursts significantly increased with continuous VLL stimulation at 50 Hz and an even greater increase occurred with VLL stimulation at 80 and 100 Hz (**Figure 6d**).

Overall, these results demonstrate that VLL stimulation can potentiate motor output even in the presence of hemiparesis caused by lesions located within the CST.

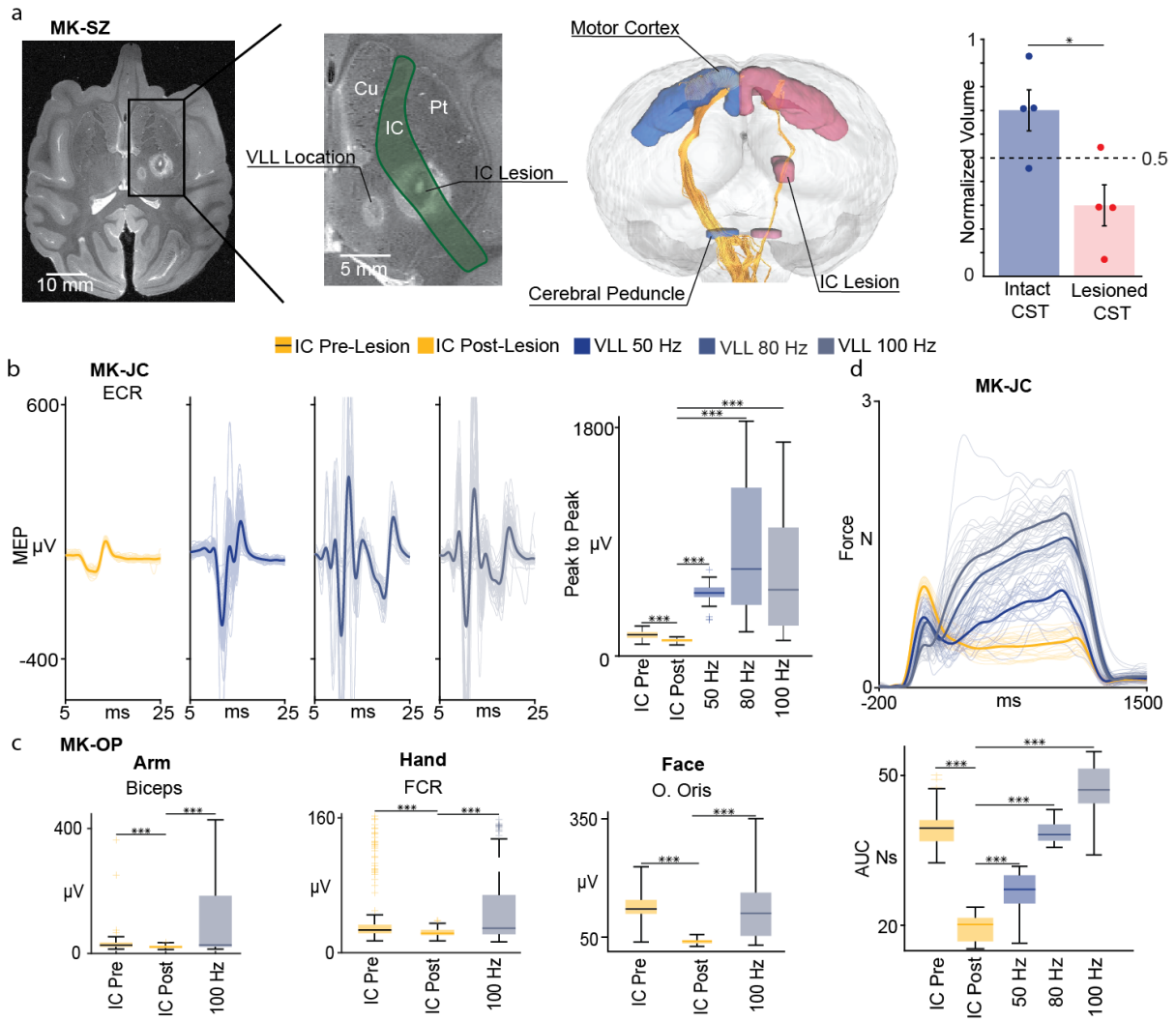

Figure 6: DBS amplifies motor outputs after CST lesions.
(a) *Left:* T2-weighted post-mortem MRI of IC lesion and VLL location (axial plane). (Cu: Caudate Nucleus, IC: Internal Capsule, Pt: Putamen). *Center:* HDFT of the corticospinal tract (CST) in intact and lesioned hemispheres. *Right:* volume of CST (mean +- standard error over animals) for both hemispheres normalized over the sum of the volumes in both hemispheres. **(b)** Example of post-lesion MEPs of one hand muscle (n=40, ECR: Extensor Communis Radialis, Mk-JC). Boxplots of peak to peak amplitude of MEP pre- and post-lesion for IC alone, and IC with VLL 50 Hz, VLL 80 Hz and VLL 100 Hz. **(c)** Boxplot of peak to peak amplitudes of MEPs in one arm muscle (Biceps), one hand muscle (EDC: Extensor digitorum communis), and one face muscle (Orbicularis Oris) for pre- and post-lesion for IC alone, and IC with VLL 100 Hz. **(d)** *Top*: Example of force traces (n=20). *Bottom*: boxplot of AUC pre- and post-lesion for IC alone, and IC with VLL 50 Hz, VLL 80 Hz, and VLL 100 Hz. For all panels, statistical significance was assessed with one-tail bootstrapping with Bonferroni correction: $p<0.05$ (*), $p<0.01$ (**), $p<0.001$(***).

Motor thalamus DBS potentiates motor output in humans

We sought to verify the translational capabilities of our DBS method in human subjects. For this, after obtaining informed written consent, we performed intraoperative neurophysiological experiments in human subjects (n=4, 2 male, 2 female) who underwent surgical DBS implantation of the motor thalamus for the treatment of Essential Tremor (ET) (**Figure 7a**). Experiments were

designed to closely mimic the animal study protocols. The human motor thalamus nuclei comparable to the VLL nucleus are the ventralis intermediate (VIM) and the ventralis oralis posterior (VOP) nuclei. Indeed, HDFT analysis confirmed preferential anatomical projections from the VIM/VOP to M1 (**Figure 7b**). Additionally, we tested the connectivity of these pathways using evoked potential methods. For this, we implanted a 6-channel subdural strip electrode (Adtech, Oak Creek, WI, USA) over the upper-limb representation of the primary motor and somatosensory cortices. To confirm electrode placement, we used the validated clinical technique of somatosensory evoked potential (SSEP) phase reversal (PR) mapping[46] to locate both the hand representation of S1 cortex (largest amplitude N20/P30 cortical SSEP) and the approximate location of the central sulcus, where the polarity of the SSEP reverses (**Figure 7a**). We then mapped the upper extremity representation of primary motor cortex at the precentral gyrus by direct cortical stimulation (DCS) of the electrode contacts that were anterior to the SSEP PR. MEPs were recorded from six contralateral upper extremity muscles (Deltoid, Biceps, Triceps, Flexor carpi, Extensor carpi and APB). The strip electrode was adjusted so that the lowest threshold (~6-12 mA) MEPs were recorded from at least three UE muscles, and the electrode was fixed in place.

We then examined the projections from VIM/VOP to S1 and M1 upper extremity representations by recording cortical evoked potentials at each of the 6 electrode contacts in response to low frequency (2 or 10 Hz) stimulation of the VIM/VOP DBS electrode (Boston Scientific) implanted in the same hemisphere at the AC/PC plane (X: 12mm lateral to the AC/PC line, Y: 6mm anterior to PC, Z: 0mm to the AC/PC horizontal plane, **Extended Data Figure 8**). Cortical evoked potentials, occurring within 20 ms after the stimulus, were recorded at the M1 contacts (rostral to the PR location) (**Figure 7c**). In all subjects but one, the peak to peak amplitude of these evoked responses was significantly larger for precentral contacts than for postcentral contacts. This supports orthodromic synaptic transmission through thalamocortical projections from VIM/VOP to the hand/arm representation of the motor cortex as was observed in monkeys during stimulation of the VLL.

Next, DCS MEPs from up to six contralateral upper extremity muscles were recorded with and without paired VIM/VOP DBS stimulation at 50, 80, or 100 Hz. Similar to the monkey experiments, we observed a consistent increase in the DCS MEP amplitudes across arm, wrist and hand muscles with VIM/VOP stimulation at 50 Hz compared to DCS alone. A more variable behavior was found with VIM/VOP stimulation at higher frequencies (100 Hz, **Figure 7f**). Indeed, when quantifying the effect of VIM/VOP stimulation across stimulation frequencies and muscles, we found that 50Hz DBS consistently enhanced muscular responses in a statistically significant way, whereas higher frequencies such as 80 and 100 Hz might further amplify or suppress these responses (**Figure 7g**, **Extended Data Figure 9**). Finally, we confirmed that similar to the monkey' experiments, electrical stimulation of the VIM/VOP alone did not produce motor evoked potentials in the arm, wrist, nor hand muscles (**Figure 7d**).

Overall, these results observed in human subjects were equivalent to those obtained in monkeys, demonstrating the translational potential of our approach and associated mechanisms of action.

Specifically, electrical stimulation of the motor thalamus enhanced motor cortex excitability and consequently potentiated motor output via the CST in human subjects.

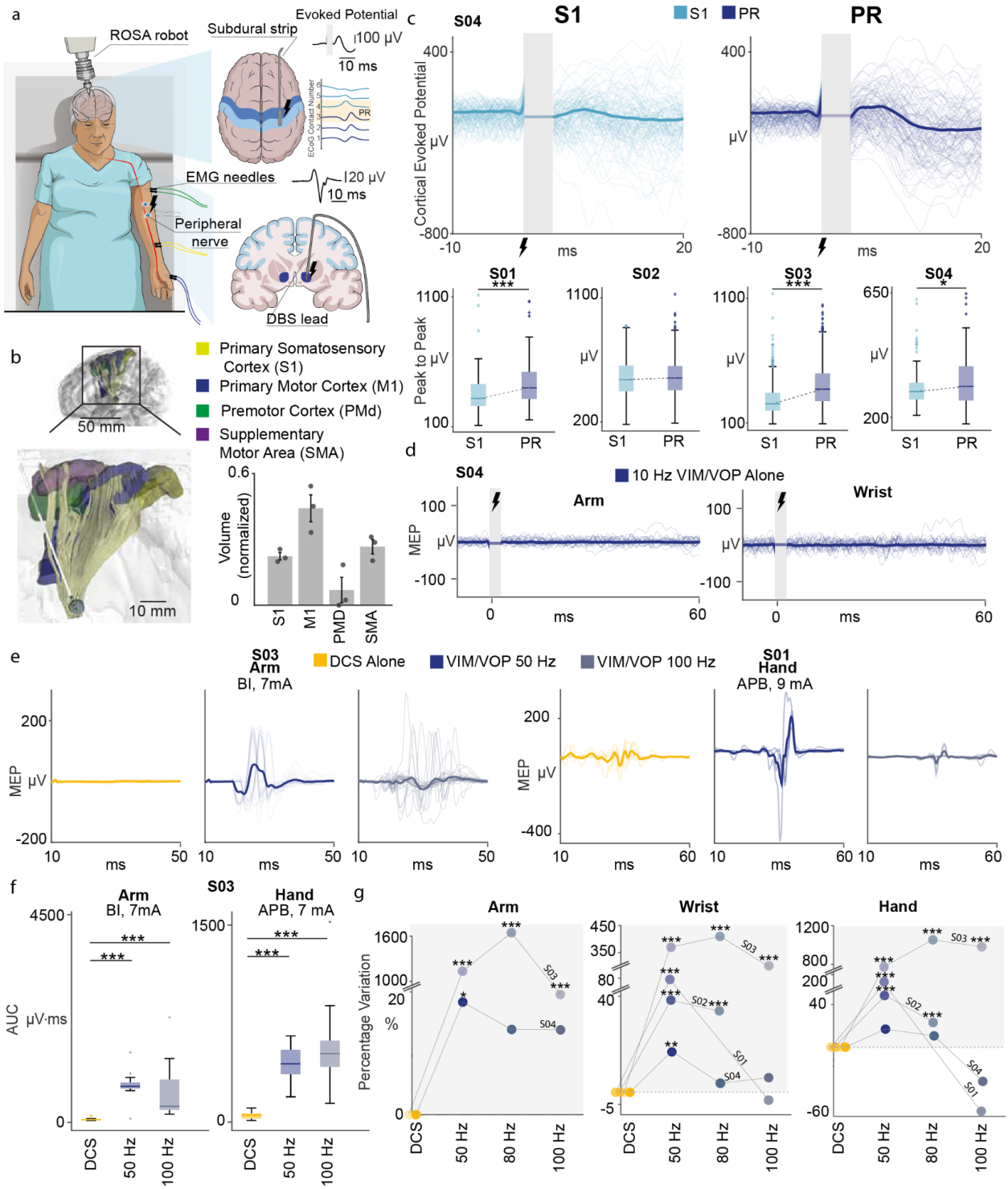

Figure 7: DBS amplifies motor outputs in humans

(a) *Top:* Experimental setup for human intraoperative DCS experiments. Enlargement shows a schematic representing the subdural strip electrode placement over the primary motor (M1) and somatosensory (S1) cortices, and the phase reversal (PR) to identify the central sulcus. Needle electrodes were inserted in arm, wrist, and hand muscles to record MEPs and superficial electrodes were placed over the median nerve for SSEP. **(b)** *Left:* HDFT from the VIM/VOP to cortical regions. *Right:* Normalized volume (mean ± standard error over n=4 subjects) of VIM/VOP projections to each cortical region normalized by the total volume of fibers. **(c)** *Top:* Example traces (n=122) of cortical evoked potentials elicited by VIM/VOP stimulation recorded over an S1 (left) and PR (right) contact for one subject (S04). *Bottom:* Box-plots of peak to peak amplitude of cortical evoked potentials at S1 and PR contact. From left to right, subjects 1 to 4 are shown (n=128, n=585, n=601, n=122 trials, respectively). **(d)** Example MEP traces (arm, biceps; wrist, flexor; n=60) with VIM/VOP stimulation alone for S03. **(e)** Example MEP traces with DCS alone and DCS paired with VIM/VOP stimulation at 50 and 100 Hz. Arm is S03 biceps (from left to right, n=48, n=60, n=60), hand is S01 abductor pollicis brevis (from left to right, n=20, n=16, n=20). **(f)** Box plots of AUC for MEPs of the arm and hand (biceps and abductor pollicis brevis respectively; n=58) with DCS alone and DCS paired with VIM/VOP stimulation at 50 and 100 Hz. **(g)** Scatter plots for arm, hand, wrist, and hand muscles of all subjects, representing the percentage of AUC variation, with respect to DCS alone, for all the different VIM/VOP stimulation frequencies (50, 80 and 100 Hz). For all panels, statistical significance was assessed with one-tail bootstrapping with Bonferroni correction: $p<0.05$ (*), $p<0.01$ (**), $p<0.001$(***).

Motor thalamus DBS increases motor output after TBI

Finally, we had the opportunity to test our hypothesis in a patient who had suffered a severe traumatic brain injury as a consequence of a motor vehicle accident (**Figure 8a**). The severe trauma resulted in bilateral diffuse axonal injury to the CST, cerebral peduncles, and pons. Consequently, TBI01 suffered from hemiparesis and tremor of the right and left upper extremities. Functionally, TBI01 required maximal assistance for eating, grooming, bathing, and dressing. With the clinical goal of treating the post-traumatic tremor, TBI01 was implanted with bilateral DBS electrodes in the VIM/VOP using standard stereotactic coordinates (X: 12mm lateral to the AC/PC line, Y: 6mm anterior to PC, Z :0mm to the AC/PC horizontal plane, **Extended Data Figure 8**). As was the case in the non-TB subjects, a 6-contact subdural strip electrode was implanted over S1 and M1 cortex of the left hemisphere (i.e., greater TBI damage). DCS MEPs were consistently recorded from the APB and flexor muscles of the hand and wrist (**Figure 8c**, left panels). Consistent with the non-TBI subjects, stimulation of the VIM/VOP nucleus resulted in larger amplitude cortical evoked potentials over motor cortical areas as compared to somatosensory cortex (**Figure 8b**). We then paired DCS of M1 with DBS of the motor thalamus to assess the effect of VIM/VOP stimulation on the hemiparetic arm. Again, DCS MEPs were significantly larger with concurrent stimulation of the motor thalamus at 50Hz and modulated in a frequency-dependent manner (**Figure 8c**, right panels). Indeed, 100 Hz stimulation resulted in suppression of MEPs, demonstrating the consistency of our findings across monkeys, non-TBI subjects, and a patient suffering from a chronic (> 6 months) CST injury.

Motor thalamus stimulation improves voluntary force control

Finally, to assess whether DBS of the motor thalamus achieves functional improvements for patients with chronic motor deficits, we tested the effect of VIM/VOP DBS in TBI01 during a functional task over several testing sessions using the chronically (> 5 months) implanted DBS system. After informed consent (University of Pittsburgh IRB) was obtained, TBI01 performed an isometric roadway test to measure his voluntary force control with and without bilateral VIM/VOP

stimulation at 55 Hz. The task involved matching grip force to a time series of thresholds, gradually increasing, sustaining, and decreasing the force between set percentages of maximum voluntary force levels that were established when DBS was OFF (**Figure 8d**). This experiment mimics those performed in anesthetized monkeys (**Figure 3c** and **Figure 6**). Across multiple days of testing (n =2 sessions), when the stimulation was turned ON at 55 Hz, TBI01 was able to reduce the amount of grip force deviation compared to when the stimulation was OFF. DBS-ON performances were smoother and more accurate when compared to DBS-OFF (**Figure 8e**, RMSE, Day 1: 0.05 (DBS ON) vs 0.07 (DBS OFF), Day 2: 0.05 (DBS ON) vs 0.14 (DBS OFF)). Importantly, the tremor was consistent with and without stimulation at 55 Hz demonstrating that the improved voluntary control was not caused by a reduction in the level of tremor (**Figure 8f**). Additionally, these effects persisted regardless of the testing order of DBS-ON and DBS-OFF, and they were therefore not induced by learning effects.

While preliminary, these results suggest that motor thalamus DBS at optimal stimulation frequencies (50-100Hz) can be applied to improve volitional fine motor control in patients with chronic lesions of the CST.

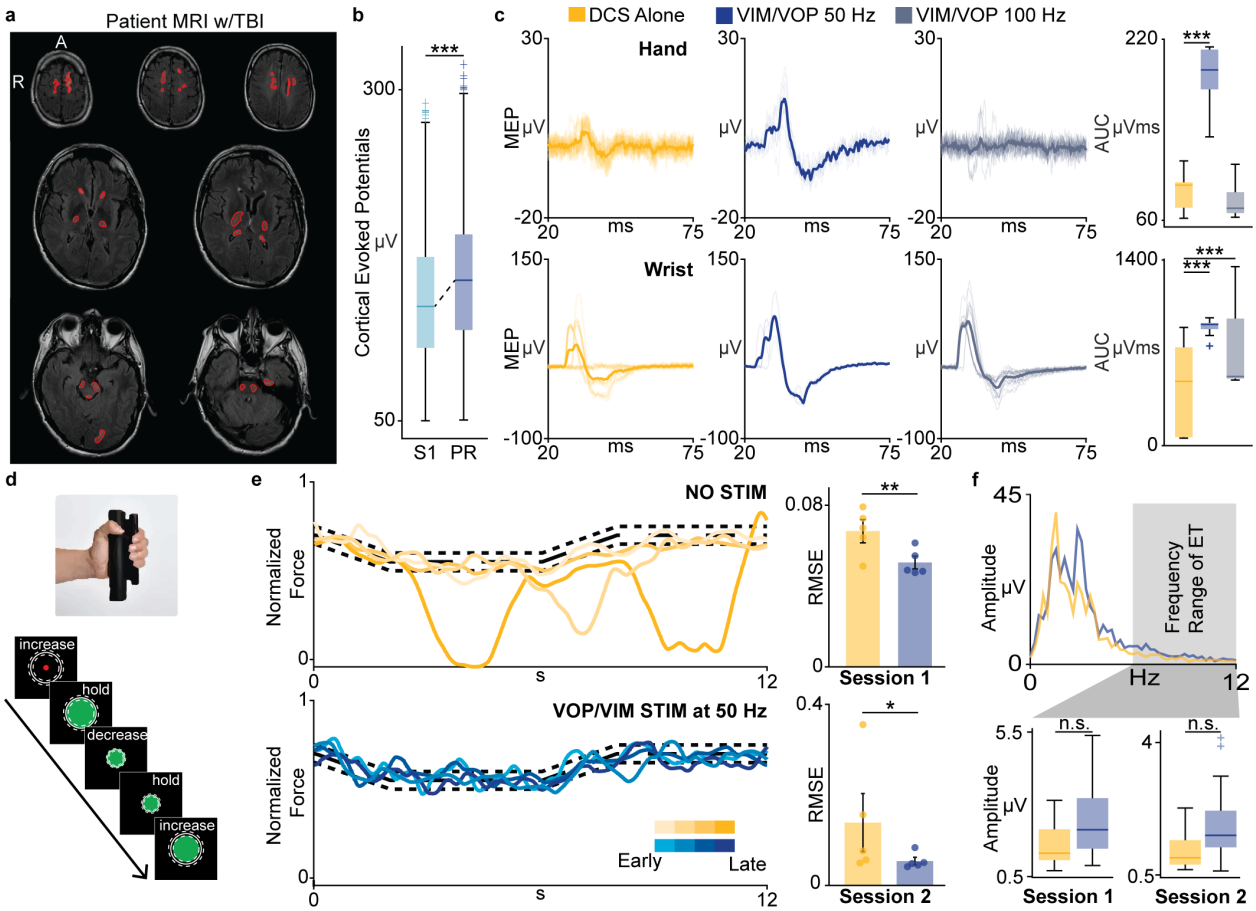

Figure 8: DBS improves voluntary motor control after TBI.
(a) MRI of TBI01 with segmented lesions in red. **(b)** Box-plots of peak to peak amplitude of cortical evoked potentials over S1 and PR contact from VIM/VOP stimulation at 10 Hz (n = 599). **(c)** *Left:* Example of MEPs

with DCS alone and DCS paired with VIM/VOP stimulation at 50 (n = 18) and 100 Hz (n = 40) for hand (APB) and wrist (EDC). *Right:* box plots of MEPs AUC of ABP and EDC (n=58) with DCS alone and DCS paired with VIM/VOP stimulation at 50 (n = 18) and 100 Hz (n = 40). **(d)** Schema of the motor task performed by TB01. **(e)** *Left*: Example of force traces without (*top*) and with (*bottom*) VIM/VOP stimulation at 55 Hz. *Right*: bar plot of the root-mean-square error of the force without (yellow) and with (blue) VIM/VOP stimulation at 55 Hz. **(f)** *Top*: average power spectrums from 1 to 12 Hz calculated over the hold periods of the task without (yellow) and whit (blue) stimulation at 55Hz. *Bottom*: boxplots of the average power spectrum over the clinical observed range for ET (6-12Hz)[47]. For all panels, statistical significance was assessed with one-tail bootstrapping with Bonferroni correction: $p<0.05$ (*), $p<0.01$ (**), $p<0.001$(***).

DISCUSSION

In this study we demonstrated with experiments in both monkeys and human subjects that DBS of the motor thalamus facilitates the recruitment of cortico-spinal neurons within the motor cortex which in turn increases motor output in paretic limbs after lesions of the CST. These results offer promising albeit preliminary support for the testing of DBS of the VIM/VOP as a therapy to improve motor deficits in people with lesions of the CST.

Identification of optimal DBS stimulation parameters is often guided by trial and error in consequence of the lack of understanding of the underlying neural mechanisms[14,48]. To overcome this situation, here we designed experiments aimed at identifying the mechanisms mediating the increase in motor cortex excitability in order to guide the design of optimal stimulation strategies. By combining intra-spinal and intra-cortical electrophysiology in monkeys and humans we verified that DBS of motor thalamus increased motor output by augmenting the recruitment of cortico-spinal motor neurons within the primary motor cortex via excitatory synaptic inputs from the targeted thalamic nuclei. Synaptic-mediated excitatory inputs are known to be less efficient at high stimulation frequency because of presynaptic inhibitory effects such as depletion of neurotransmitters and presynaptic inhibition[14,41,49–52]. For this reason, we explored lower than clinically used frequencies which led us to confirm that the 50-100 Hz range was optimal to sustainably increase motor output. This range is different from commonly used DBS stimulation frequencies (> 130 Hz)[44] at which instead we found frequent *suppression* of motor output. This demonstrated the importance of understanding the mechanisms of action to tailor DBS to our specific application[14,48,53]. In fact, a few previous studies had already investigated the use of DBS to treat post-stroke muscle weakness and paresis[54–58]. However, limited understanding of the underlying mechanisms of stimulation led to suboptimal choices of the implant location and stimulation protocols affecting size and consistency of the observed effects.

DBS of the VIM/VOP facilitated M1 DCS MEPs in the upper extremity muscles via the CST and enhanced grip forces, which suggests that this therapy could be effective in restoring motor functions by addressing two of the main symptoms after damage to the CST: muscle weakness and loss of strength[9,59]. Indeed, our method availed a fully implanted TBI patient to volitionally modulate grip force, demonstrating that continuous DBS improves fine motor control. In our preparation, we could not test whether VIM/VOP-DBS reduces upper-limb spasticity, i.e., another symptom often observed with upper motor neuron syndrome. However, previous case studies demonstrated effectiveness of motor thalamus DBS in reducing spasms in dystonia patients[60], suggesting that the method could be translated for stroke- or TBI-induced spasticity. Finally, in

addition to increased motor output of hand and arm muscles, DBS of the VIM/VOP induced MEP potentiation of face muscles suggesting that our approach could potentially improve speech motor deficits such as dysarthria and apraxia.

Interestingly, the observed effects appeared immediately upon turning on thalamic stimulation and stopped as soon as it was turned off, suggesting an “assistive power” of thalamic DBS. Here we placed an emphasis on optimizing the thalamic stimulation parameters to maximize these immediate assistive effects. In fact, several studies have shown that non-invasive brain stimulation of the ipsilesional motor cortex using transcranial magnetic stimulation (TMS) or transcranial direct-current stimulation (tDCs) enhanced cortical excitability and improved long-term motor functions after stroke[61–69]. We could, therefore, hypothesize that the DBS-mediated increased motor cortex excitability would have an immediate therapeutic effect with DBS on and the potential for persistent long-term motor recovery in the absence of DBS stimulation. Additionally, the assistive effects of DBS may enable patients to engage in exercises that they would not otherwise be able to perform, promoting the advent of DBS-combined behavioral interventions. Along these lines, previous works combined TMS or tDCs with behavioral training enhancing the effects of brain stimulation alone[70–75]. Similar considerations could apply to motor thalamus DBS. Finally, the therapeutic effects of VIM/VOP-DBS might be more clinically relevant when compared to non-invasive cortical stimulation because of the higher selectivity[14,15] and continuous nature[59] of DBS, akin to DBS therapy in patients with Parkinson’s disease and Essential Tremor. In fact, non-invasive systems cannot be implanted and consequently be utilized all day. The continuous nature of the DBS stimulation, instead, would enable daily use of the paretic limb possibly driving further plasticity.

Critically, the VIM/VOP target is commonly used as a target for DBS therapy in clinical practice for the treatment of Essential Tremor, and the devices used in this study are commercially available, FDA approved, and currently implanted in more than 12,000 patients per year for the treatment of different movement and psychiatric disorders[14]. Importantly, procedure- and hardware-related adverse events of DBS implantation are extremely low (<0.5% of patients)[76]. Moreover, surgical risk in patients with a history of stroke or TBI can be minimized by careful pre-operative management of anticoagulants and by delaying the implantation for at least three months following the brain insult[77,78]. This was recently demonstrated in a large clinical trial (n=108) deploying vagus nerve stimulation to treat post-stroke motor deficits[79]. Therefore, the surgical intervention required for motor thalamus DBS implantation does not represent a significant barrier to its clinical translation to treat subcortical stroke or TBI.

The most important limitation of this study is that the behavioral tests in humans were performed in only one TBI patient. However, the main goal of this work was to first identify the mechanisms of action of thalamic DBS to optimize stimulation targets and parameters and quantify the immediate assistive effects. We extensively performed these investigations in a large number of monkeys and non-TBI subjects which, combined to the results of TBI01, support the extension of this study towards a larger cohort of patients with CST lesions. Secondly, although we explored mainly the effects of stimulation of the VIM/VOP (or VLL in monkeys) nucleus, we cannot rule out the presence of other subcortical targets with excitatory projections to the motor cortex, such as the centromedian thalamic nucleus, that could have similar effects. However, our choice was

driven by the well-established surgical approach to implant DBS into the VIM/VOP for ET treatment.

In conclusion, based on a progressive series of experiments from non-human primates to human subjects, we argue that our optimization of motor thalamus DBS to enhance motor outputs could unlock a realistic and effective therapy for motor related deficits after CST lesions. Future studies in multiple patients with stroke or TBI are now necessary to demonstrate this possibility.

ACKNOWLEDGEMENTS
We thank Isabella Bushko for the design of figure elements, Dr. Amr Mahrous for providing support during the monkey surgeries, and Christopher Pappas for helping with the VIM/VOP stimulation during the human surgeries. We wish to thank Zimmer Biomet for lending the ROSA robot to use in our surgeries (we declare no conflict of interest). We would like to thank Merek Gourley for providing post-implant reconstructions of the DBS patients. The study was executed through the support of internal funding from the Department of Physical Medicine and Rehabilitation at the University of Pittsburgh to EP. Additionally, this research was partially supported by the Walter L. Copeland Foundation to EP and MC, the Hamot Health foundation to JGM, and the National Institute of Health: R01NS122927-01A1 to JGM. Additional funding was provided by the Department of Neurological Surgery at the University of Pittsburgh to MC and JGM.

AUTHORS CONTRIBUTIONS
EP and JGM conceived the study. EP, JGM, and MC secured funding. JH, EG, DC, MC, JGM, and EP designed the experiments. JH, EG, JB, LL, MC, and EP designed and implemented hardware and software for the monkey experiments. JH and LL performed the image processing for all the monkeys' experiments. TKH collected the monkeys' imaging data. JH, LL, and JBM processed the DTI data for both the human and the monkeys. JH and SK processed the deep lab cut data for the kinematic analysis of the monkeys. JH, LL, JGM and EP designed the neurosurgical approach for the brain implants and JGM performed the surgery. JH, LL, JB, PG and MC designed the neurosurgical approach for the spinal implants and PG performed the surgery. VK and DF assisted with all monkeys' surgeries. TC and JGM implemented patient recruitment, eligibility and monitoring and coordinated study management. JH, EG, AD, and EP collected all human and monkey data with the assistance of JB, LL, and MC for the monkeys' experiments. DC performed the subcortical mapping of VIM/VOP for the human DBS implantations. GMA and DC collected the electrophysiology human data. JH, EG and AD analyzed the data. EP, JGM, MC and DC helped with data interpretation. EP, JGM, JH, EG and AD wrote the paper and all authors contributed to its editing.

CONFLICT OF INTERESTS
The authors declare no conflicts of interests in relation to this work.

DATA AND MATERIALS AVAILABILITY
All software and data will be available upon reasonable request to the corresponding author.

Extended Data Figures:

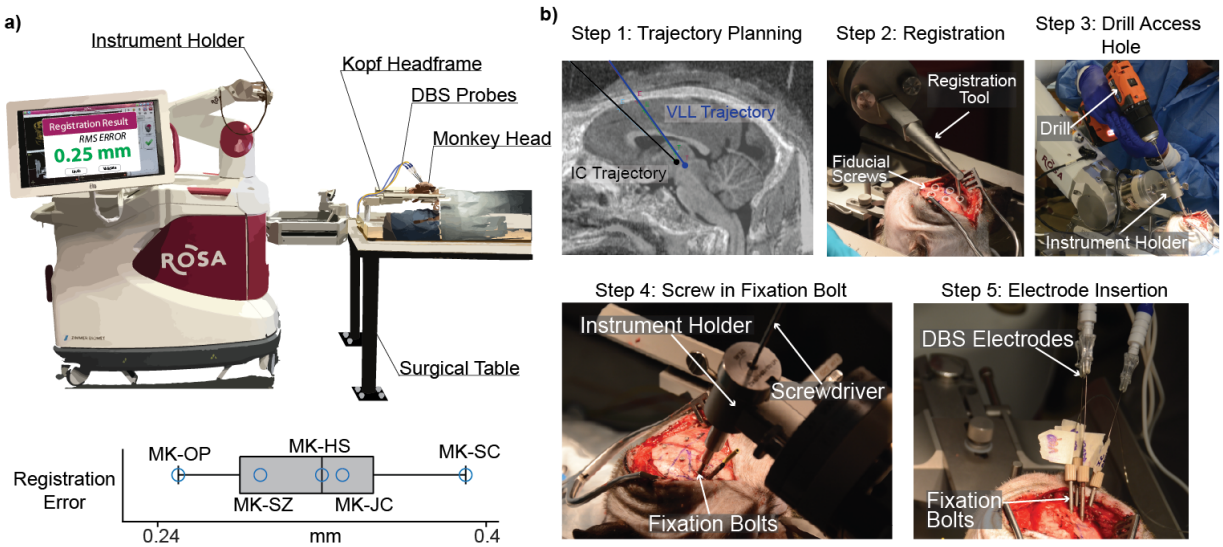

Extended Data Figure 1: ROSA Setup/Implantation Steps.
(a) *Top*: Rosa robot surgery setup. This panel was adapted from[36]. *Bottom*: Root mean squared registration error after registration using the fiducial screws **(b)** Step 1: we plan the trajectories of each DBS probe in the ROSA One Brain planning software. Step 2: using the Rosa registration tool, we register the position of the brain with fiducial screws in the skull. Step 3: an access hole is drilled into the skull along the trajectory of the probe. Step 4: fixation bolts are screwed into the skull along the probe trajectory. Step 5: DBS and IC electrodes are inserted into fixation bolts at target depth.

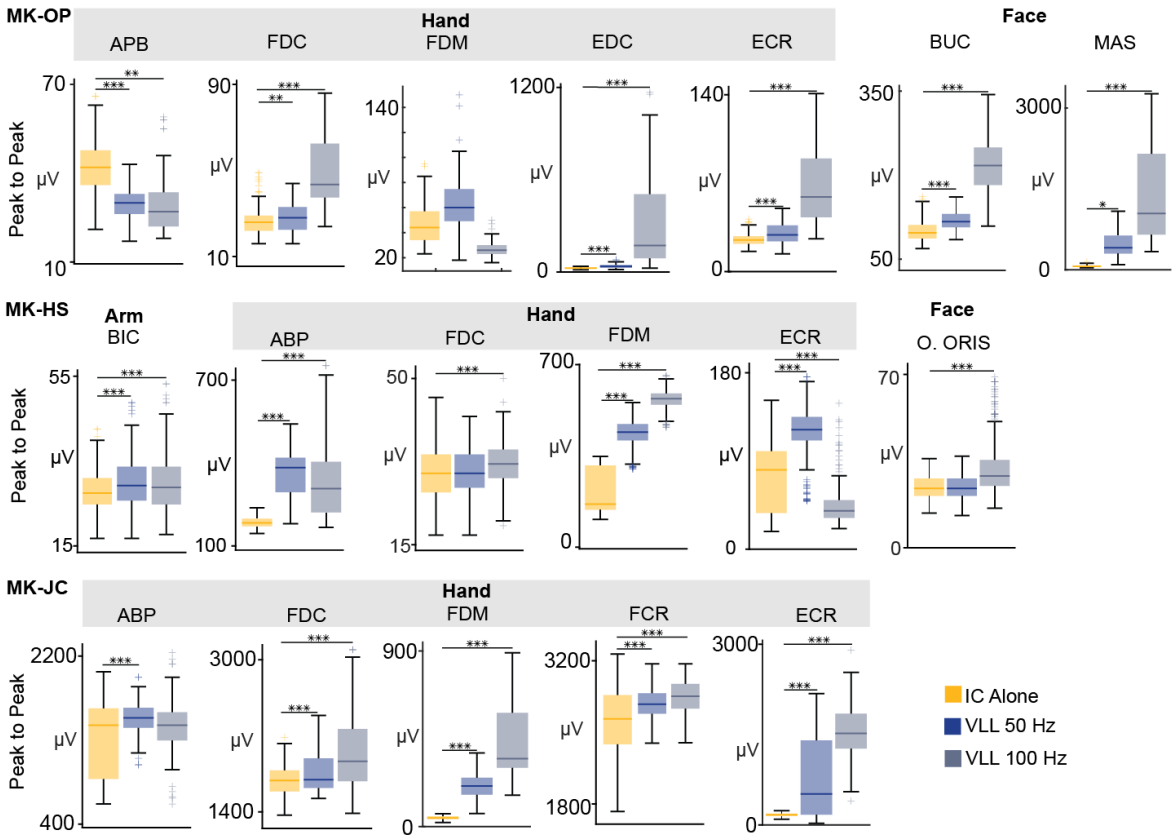

Extended Data Figure 2: VLL Stimulation amplifies MEP across arm, hand, and face muscles. Boxplots of peak to peak amplitude of MEPs across multiple muscles (APB: Abductor Pollicis Brevis, FDC: Flexor Digitorum Communis, FDM: Flexor Digiti Minimi, EDC: Extensor Digitorum Communis, ECR: Extensor Carpi Radialis, BIC: Biceps, Buc: Buccinator, Mas: Masseter, O. Oris: Orbicularis Oris) in n=3 animals (MK-OP, MK-HS, MK-JC) where EMG recordings were performed. MEPs were recorded during IC stimulation alone and then paired with VLL stimulation at 50 Hz and 100 Hz. For all panels, statistical significance was assessed with one-tail bootstrapping with Bonferroni correction: $p<0.05$ (*), $p<0.01$ (**), $p<0.001$(***).

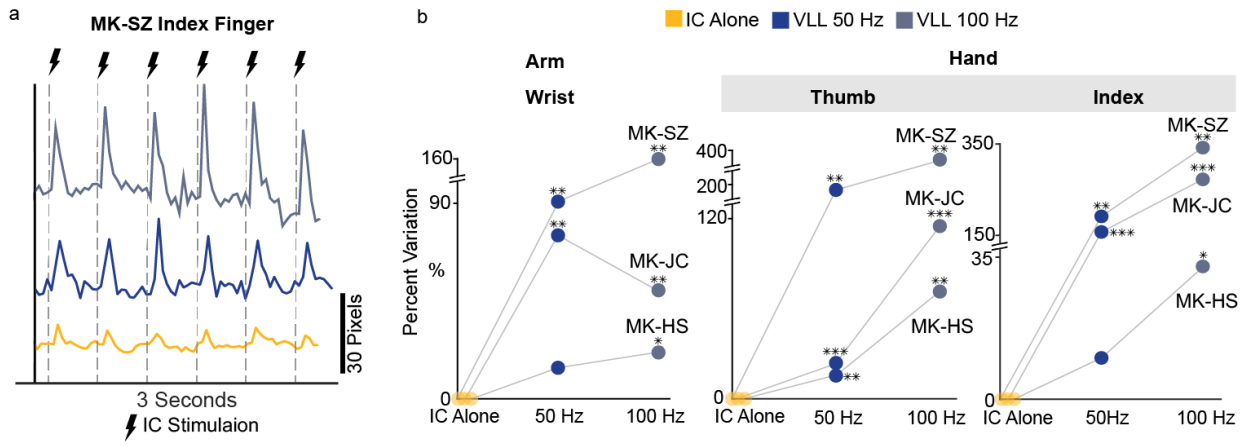

Extended Data Figure 3: VLL stimulation potentiates movements of the arm and hand.
(a) Example kinematic trace from MK-SZ with IC alone and paired with VLL stimulation at 50 Hz and VLL at 100 Hz. **(b)** Scatter plots for the arm (wrist marker) and hand (thumb and index marker), representing the percentage variation of the peak to peak amplitude, in n=3 animals (MK-SZ, MK-HS, MK-JC). Kinematics were recorded during IC stimulation alone and then with paired VLL stimulation at 50 Hz and 100 Hz. For all panels, statistical significance was assessed with one-tail bootstrapping with Bonferroni correction: $p<0.05$ (*), $p<0.01$ (**), $p<0.001$(***).

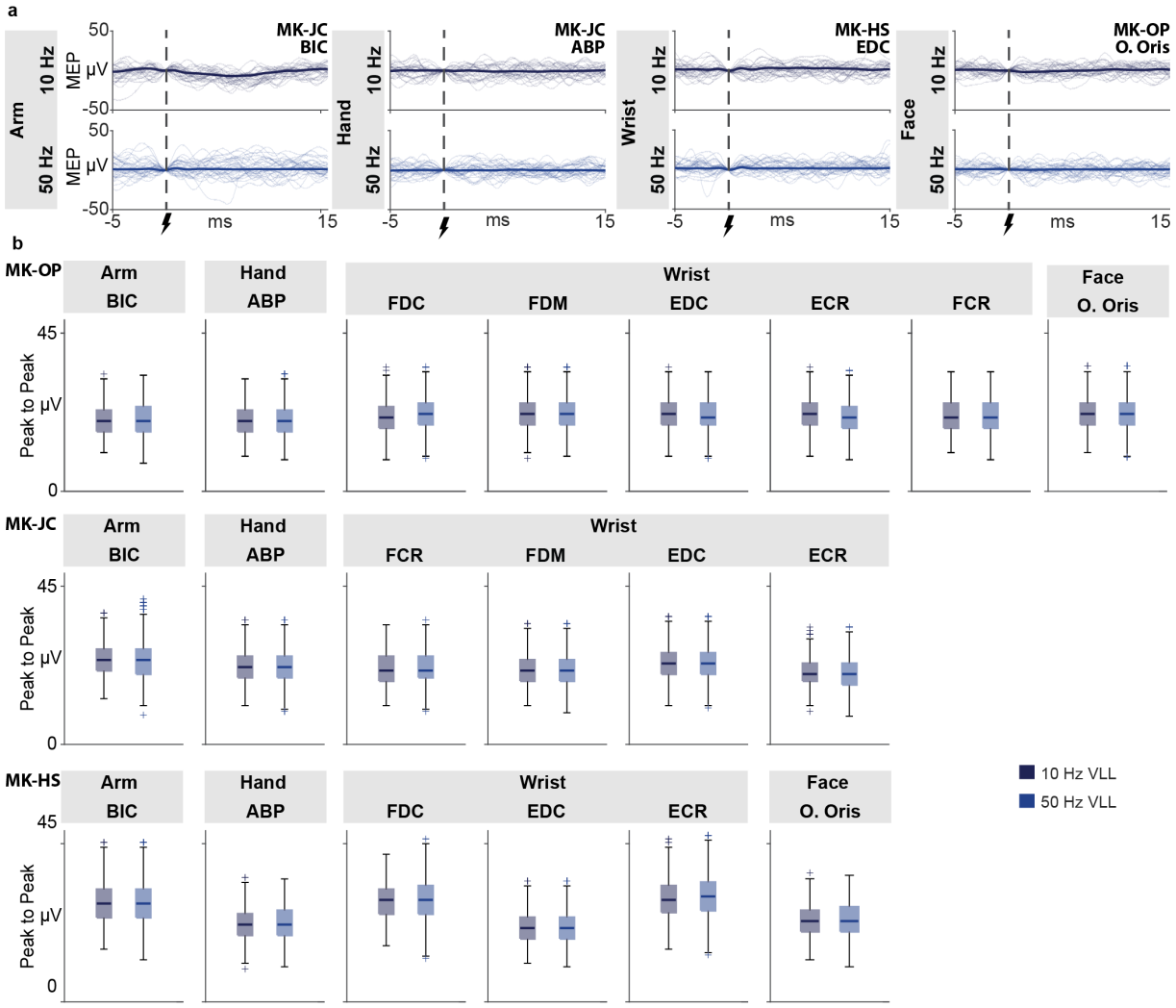

Extended Data Figure 4: MEP responses from VLL stimulation.

(a) Example MEPs (30 traces for each plot) of one arm, hand, wrist, and face muscle elicited by VLL stimulation at either 10 Hz (*top row*) or 50 Hz (*bottom row*). **(b)** Boxplots of the peak to peak MEP responses to VLL stimulation at 10 and 50 Hz for arm (BIC: Bicep), hand (ABP: Abductor Pollicis Brevis and APL: Aductor pollicis longus), wrist (ECR: Extensor Carpi Radialis, EDC: Extensor Digitorum Communis, FCR: Flexor Carpi Radialis, FDC: Flexor digitorum superficialis, and FDM: Flexor digiti minimi brevis), and face (O. Oris: Orbicularis oris) muscles for three animals (MK-OP, MK-JC, MK-HS).

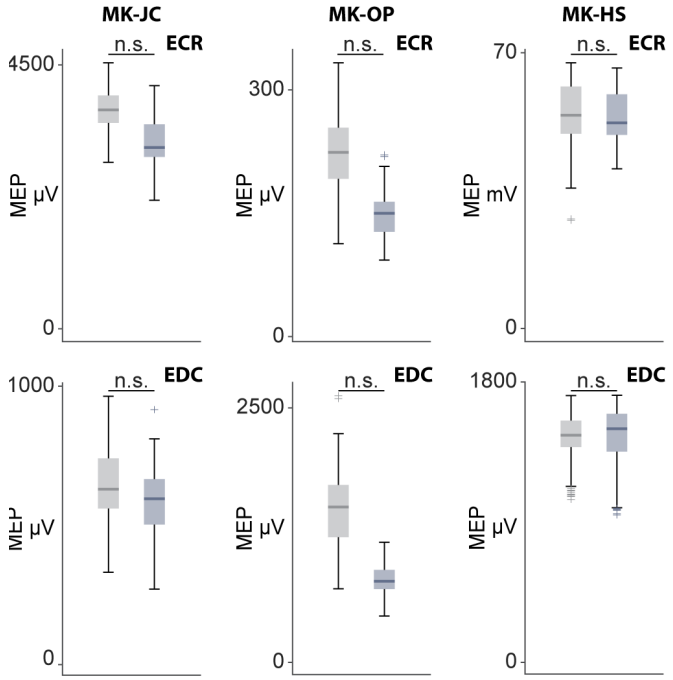

Extended Data Figure 5: Radial nerve MEPs

Boxplots of the peak to peak amplitudes of the EMG reflexes for ECR *(top row)* and EDC *(bottom row)* elicited by radial nerve stimulation alone and radial nerve stimulation paired with continuous VLL stimulation at 50 Hz for 3 animals (MK-JC, MK-OP, MK-HS). For all panels, statistical significance was assessed with one-tail bootstrapping with Bonferroni correction, however, in all cases the results were not significant.

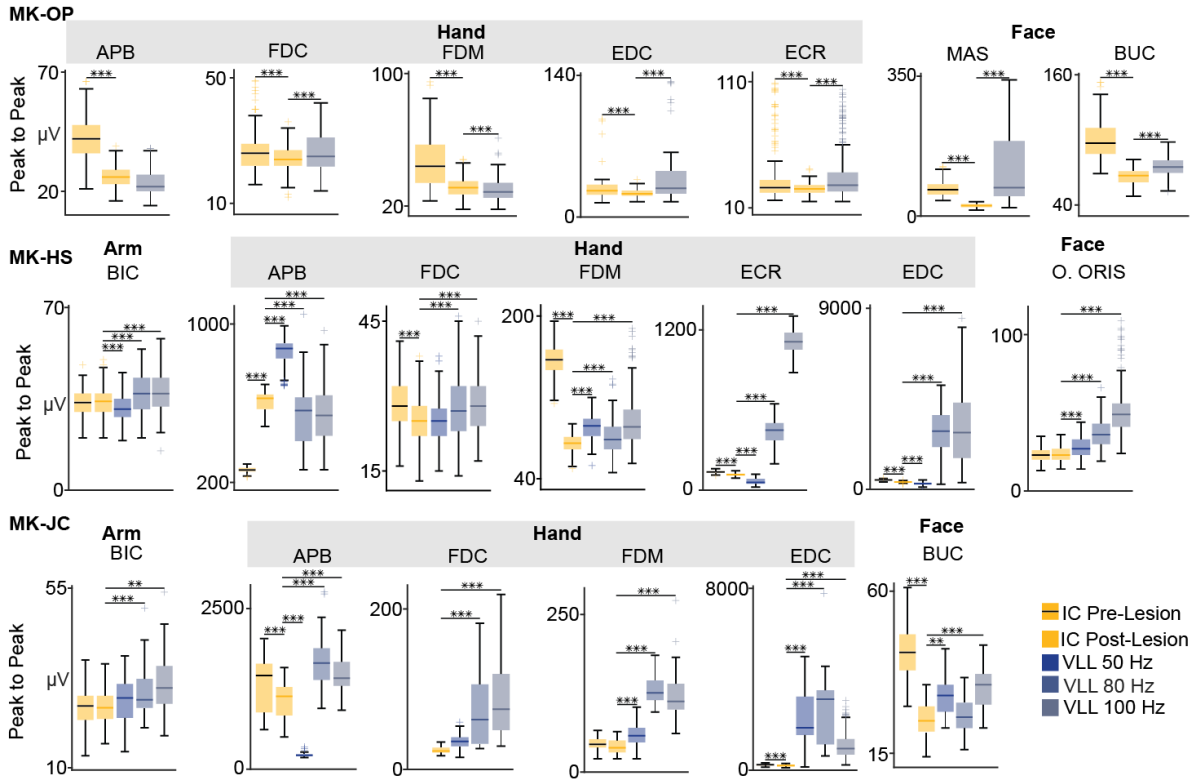

Extended Data Figure 6: Potentiation of MEP persists after CST Lesion across arm, hand, and face muscles.

Boxplots of peak to peak amplitudes of MEPs across multiple muscles (APB: Abductor Pollicis Brevis, FDC: Flexor Digitorum Communis, FDM: Flexor Digiti Minimi, EDC: Extensor Digitorum Communis, ECR: Extensor Carpi Radialis, BIC: Biceps, Buc: Buccinator, Mas: Masseter, O. Oris: Orbicularis Oris) in n=3 animals (MK-OP, MK-HS, MK-JC) where EMG recordings were performed after lesion of the CST. MEPs were recorded during IC stimulation alone before and after the CST lesion and then with paired VLL stimulation at 50, 80, and 100 Hz. For all panels, statistical significance was assessed with one-tail bootstrapping with Bonferroni correction: $p<0.05$ (*), $p<0.01$ (**), $p<0.001$(***).

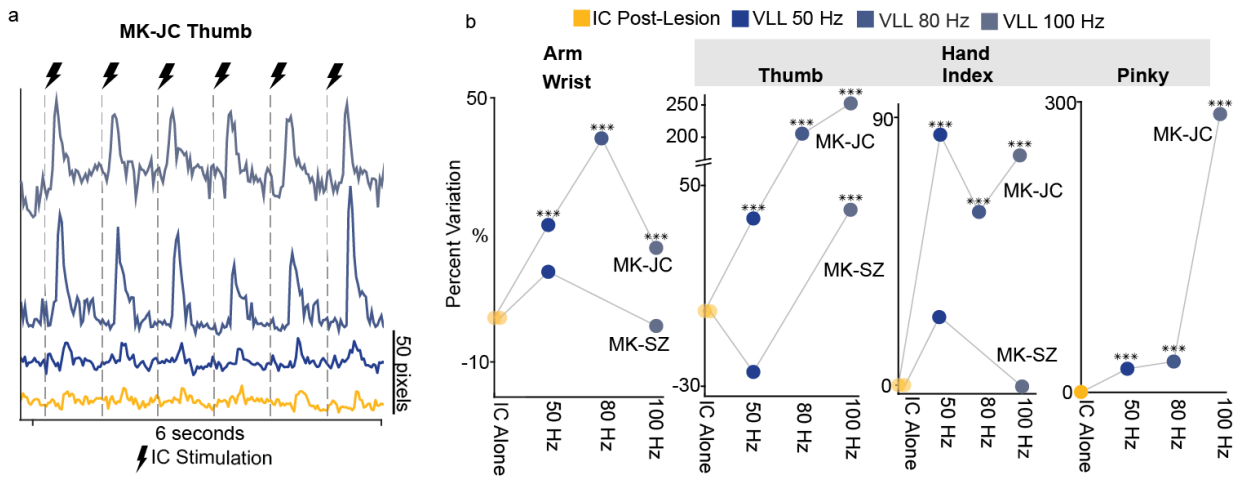

Extended Data Figure 7: Potentiation of movements persists after CST Lesion.
(a) Example kinematic trace from MK-JC with IC alone and paired with VLL at 50, 80, and 100 Hz after lesion of the CST. **(b)** Scatter plots for the arm (wrist marker) and hand (thumb, index, and pinky marker), representing the percentage variation of the peak to peak amplitude, in n=2 animals (MK-SZ and MK-JC). Traces were created in DeepLabCut with markers placed on the thumb, index finger, pinky finger, and wrist. Kinematics was recorded during IC stimulation alone and IC stimulation paired with VLL stimulation at 50, 80, and 100 Hz. For all panels, statistical significance was assessed with one-tail bootstrapping with Bonferroni correction: $p<0.05$ (*), $p<0.01$ (**), $p<0.001$(***).

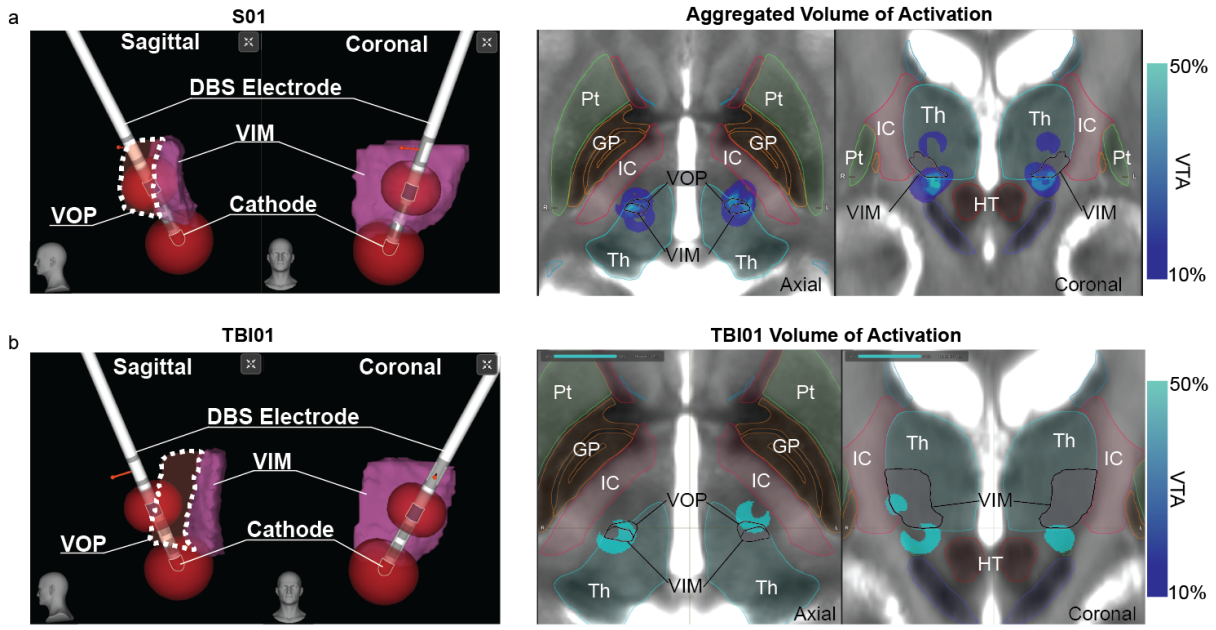

Extended Data Figure 8: Human DBS Volume of Tissues Activation.

(a) *Left*: Reconstructions of the VIM/VOP deep brain stimulation (DBS) electrode from one subject (S01). Simulated volume of tissue activation (VTA) at the cathode and anode (bipolar stimulation). *Right*: Aggregation of VTAs from n=4 human participants (S01, S02, S03, S04). **(b)** *Left*: Reconstructions of VIM/VOP DBS electrodes and VTA from TBI01. *Right*: modeled VTA from VIM/VOP DBS for TBI01.

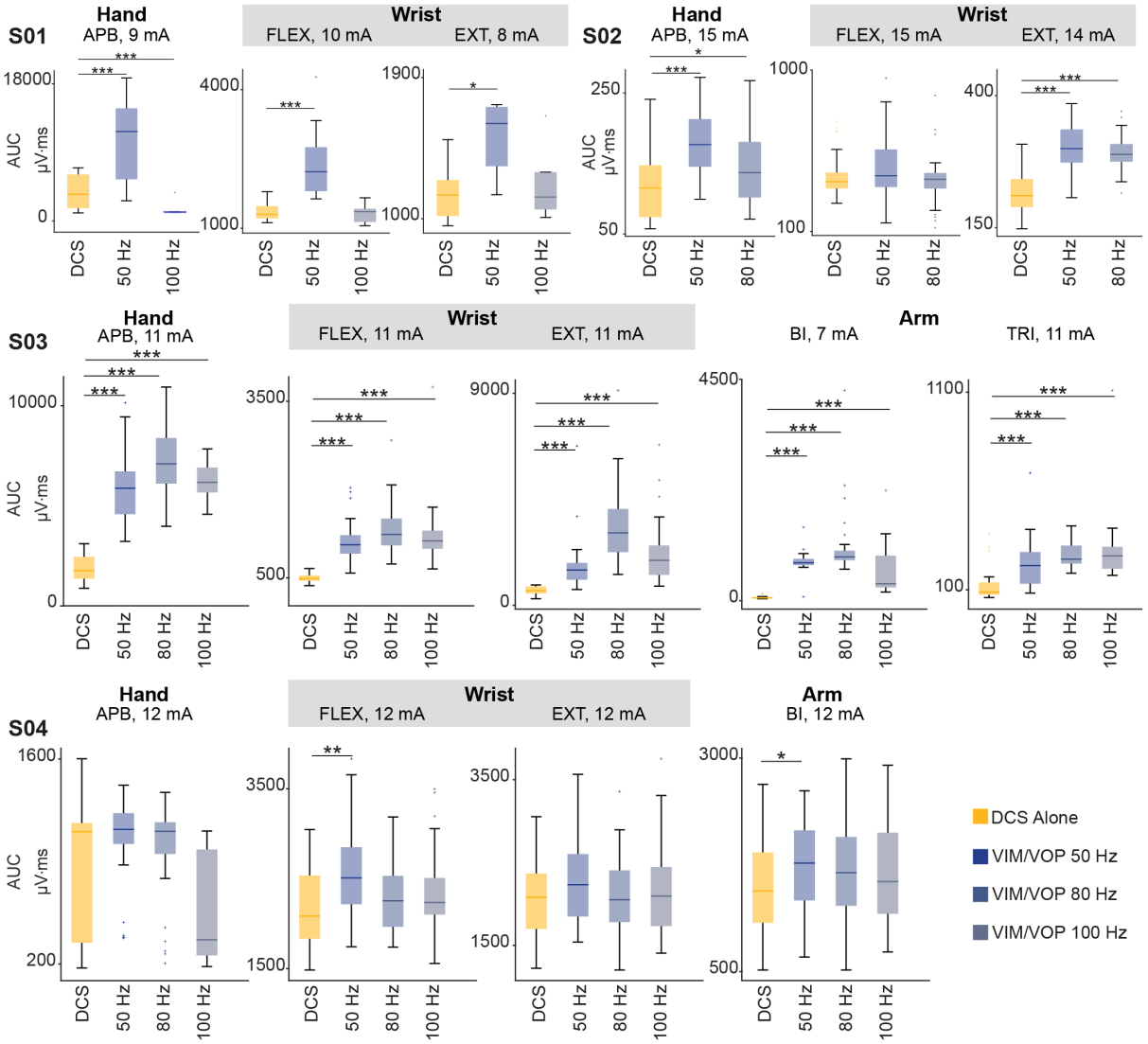

Extended Data Figure 9: DBS potentiates MEPs across arm, wrist and hand muscles in humans. Box plots of MEPs AUC amplitudes of different muscles with DCS alone and DCS paired with VIM/VOP stimulation at 50, and/or 80 Hz and/or 100 Hz. All subjects (S01, S02, S03 and S04) are reported. Amplitudes refer to the current amplitudes for DCS. APB, abductor pollicis brevis, FLEX, flexors; EXT, extensors; BI, biceps; TRI, triceps. For all panels, statistical significance was assessed with one-tail bootstrapping with Bonferroni correction: $p<0.05$ (*), $p<0.01$ (**), $p<0.001$(***).

MATERIALS AND METHODS

Animals

All procedures were approved by the University of Pittsburgh Institutional Animal Care and Use Committee (protocol number IS0017081). We utilized 4 adult Macaca Fascicularis (3 male: MK-SC 4y.o. 5.4kg, MK-SZ 4y.o. 5.9kg, MK-JC 6y.o. 8.2kg, 1 Female: MK-OP 6y.o. 6kg) and 1 adult male Macaca Mulatta (MK-HS 7y.o. 12kg). The animals were housed in the Division of laboratory Animal Resources at the University of Pittsburgh. When possible, the animals were pair housed with another animal prior to any surgical procedures. The animals were not water or food restricted and were given daily enrichments (novel food, toys, puzzles). Detailed information on which animals were involved in specific experimental procedures are reported in **Supplementary Table 1.**

Animal surgical procedure

For each animal, we performed one survival surgical procedure and one terminal surgical procedure. During the survival surgical procedure, we implanted five fiducial titanium screws (1.5mm x 4mm, KLS Martin) in the skull at non-coplanar depths. We then performed a computed tomography (CT) scan (250µm isotropic, Epica Vimago GT30) of the skull with the implanted screws. The procedure was performed using standard aseptic techniques under full anesthesia induced with ketamine (10 mg/km, i.m.) and maintained under isoflurane (1-3%, 2 L/min, inhalant). Over the next 7 days, we injected anti-inflammatory drugs once per day (Rymadyl 4mg/kg, Dexamethsasone 0.4 mg/kg).

During the terminal surgery the following procedures were performed: 1) peripheral nerve and muscle implantation, 2) robotic deep probe implantation, 3) intra-cortical electrodes arrays implantation, 4) spinal probe implantation, and 5) subcortical lesioning. These procedures were performed under full anesthesia induced with ketamine (10 mg/kg, i.m.) and maintained under continuous intravenous infusion of propofol (1.8-5.4 ml/kg/h) and fentanyl (0.2-1.7 ml/kg/h). Certified neurosurgeons performed these surgical procedures (Drs. Jorge Gonzalez-Martinez, Peter Gerszten, Daryl Fields, Vahagn Karapetyan, UPMC, Pittsburgh, USA). At the end of the experiments, the animals were euthanized with a single injection of pentobarbital (86 mg/kg) and perfused with 4% paraformaldehyde (1 L/kg) for further tissue imaging.

Peripheral nerve and muscle implantation

We dissected from the lateral epicondyle of the arm and implanted a cuff electrode (FNC-2000-V-R-A-30 bipolar nerve-cuff Micro-Leads Neuro, Ann Arbor, MI, USA) around the deep branch of the radial nerve (motor branch). We electrically stimulated two branches of the radial nerve and assessed the EMG response to verify the motor branch from the cutaneous branch. We then inserted EMG needle electrode electrodes (disposable single 13mm Subdermal needle electrode, Rhythmlink) into the extensor carpi radialis (ECR), extensor digitorum communis (EDC), flexor digiti minimi (FDM), flexor carpi radialis (FCR), flexor digitorum communis (FDC), abductor pollicis brevis (APB), and biceps (hand and arm muscles). Additionally, in n=3 animals (MK-OP, MK-HS, MK-JC), we implanted EMG electrode needles in the Masseter (Mas), Orbicularis Oris (O. oris), and Buccinator (Buc) (face muscles).

Robotic deep probes implantation

We implanted each depth electrode using the ROSA One(R) Robot Assistance Platform (ROSA robot) to allow for highly accurate implantations of the ventral laterolateral (VLL) thalamic nucleus and the hand area of the internal capsule (IC)[36]. Prior to the terminal surgery, we obtained preoperative T1-weighted magnetic resonance imaging (MRI) scan (400µm isotropic, TR/TE: 6000/3.7 ms, 7T Siemens whole body human system) and CT imaging to estimate precise targets and trajectories for each electrode. Both imaging procedures were performed with the animals secured in a customized plastic stereotactic frame to facilitate co-registration. We then co-registered MRI and CT images using ROSA One Brain Application and selected three targets: the hand area of the cortico-spinal tract (CST) within the IC at the AC-PC level (stimulating electrode), a target 2 cm ventral to create a thermal-ablation lesion (lesioning electrode), and the VLL nucleus of the motor-sensory thalamus. We planned the trajectories of the probe in the ROSA software, avoiding vasculature and the ventricles. The entrance of the probes was positioned 2 cm in front of the central sulcus to keep the motor and somatosensory cortices intact for the implantation of the intra-cortical electrode arrays. We then positioned the monkeys prone in a stereotaxic head frame (Kopf, Model 1530, Tujunga, CA, USA) and registered the ROSA robot to the monkey using the implanted fiducial screws. The robot guided the drilling of penetration holes and the precise implant of the fixation bolts. For the two probes within the internal capsule, we inserted and fixed a radiofrequency cannula (S-100 5 mm ActiveTip Straight cannula 22G, Abbott) and a radiofrequency electrode (RF-SE-10 Reusable Stainless Steel Electrode, Abbott) at the correct depth into the brain. Correct positions of the probes within the IC were estimated by recording evoked electromyography (EMG) potentials from stimulation of the IC at 2 Hz at amplitudes between 800uA and 2mA that should produce mono-synaptic activation of the cervical motoneurons. For the stimulation of the VLL, we inserted a 16 channel Dixi electrode (DIXI Microdeep® SEEG Electrodes) into its fixation bolt. Correct position within the VLL was confirmed by recording evoked potentials in the cortex during electrical stimulation (1 Hz) at amplitudes between 1 and 4.8mA that elicited clear evoked potentials in the motor cortex, but not in the somatosensory cortex. Detailed information on the amplitudes and pulse durations used for stimulation of the IC and the VLL are reported in **Supplementary Table 2.**

Intra-cortical electrodes arrays implantation

We performed a 20 mm diameter craniotomy over the central sulcus and removed the dura to expose primary motor and primary somatosensory cortices. Functional motor areas of the arm were identified through anatomical landmarks and intra-surgical micro-stimulation. The position of the primary somatosensory area (S1) was then determined in relation to the hand representation of the primary motor cortex (M1). We then implanted intracortical arrays in M1 (48 channels) and S1 (48 channels) for a total of 96 channels (400µm pitch, electrode length 1.0mm Blackrock Microsystems, Salt Lake City, UT, USA). In MK-JC, we implanted a 64-channel array into M1 and a 48-channel array into S1 (total 112 channels, 400µm pitch, electrode length 1.0mm Blackrock Microsystems, Salt Lake City, UT, USA). The arrays' implantation was achieved using a pneumatic compressor system (Impactor System, Blackrock Microsystems).

Spinal probe implantation

After the completion of the cranial surgery, we performed a laminectomy from C3 to T1 vertebrae and exposed the cervical spinal cord. We then implanted a 32-channel linear spinal probe (A1x32-15mm-100-177-CM32 Linear Probe with 32 pin Omnetics Connector, NeuroNexus, Ann Arbor, MI, USA) in the gray matter at the C6-C7 spinal segment to record spinal local field potentials and multi-unit spikes. To implant the probe, we opened the dura mater and placed a small hole in the pia using a surgical needle through which penetration of the probe with micromanipulators was possible. We implanted the probe using Kopf micromanipulators (Kopf, Model 1760, Tujuna, CA, USA).

Subcortical lesioning

We utilized a radiofrequency generator (NeuroTherm NT 1100) to create the lesions[45]. Time and temperature parameters used for the lesion for each animal are summarized in **Supplementary Table 3.** At the end of the experiments before perfusion, we also created a small lesion (60℃ for 5 seconds) in VLL through the Dixi electrode to visualize the implant location post-mortem.

Data acquisition and electrophysiology

Stimulation of the IC, VLL, and radial nerve was provided using an AM stimulator (model 2100 A-M Systems, Sequim, WA, USA). Stimulation was delivered as either single pulses or bursts of cathodal, charge balanced, symmetric square pulses. The stimulation intensity for the IC and the nerve was set for each animal at the motor threshold (i.e., when movements became visible). Detailed information on the amplitudes and pulse widths used for stimulation of the IC, the VLL, and the radial nerve are reported in **Supplementary Table 2.** All electrophysiological and neural data was amplified, digitally processed, and recorded using the Ripple Neuro Grapevine and Trellis software at a sampling frequency of 30000 Hz. Neural events were determined for each channel of the Utah arrays and linear probes by applying a broadband filter between 300 Hz and 3 kHz and setting a voltage threshold of 3 root-mean-square. LFPs were filtered between 0 and 500 Hz and then downsampled to a sample frequency of 1000 Hz.

Grasp force data acquisition

To produce a grasp motion from an anesthetized monkey (MK-JC), we stimulated the IC every two seconds with a 1 second pulse train at 47 Hz and 1 mA. We collected the grasp force data using a 6-axis low-profile force and torque (F/T) sensor (Mini40, ATI Industrial Automation, North Carolina). The sensor was powered using a multi-axis (F/T) transducer system (ATI DAQ F/T) that also calibrated the force data. The sensor was able to measure three degrees of force (+/-810 N for Fxy, +/-2400 N Fz) and torque (+/- 19Nm Txy, +/- 20Nm Tz) simultaneously. A small rod was mounted to the xy-plane of the sensor to be a grip handle for the animal and the system was secure under the animal's left arm. The force and torque data were digitized and recorded using the Ripple Neuro Grapevine and Trellis software at a sampling frequency of 30000 Hz.

Animal post-mortem High Definition Fiber Tracking (HDFT)

After perfusion, the brain was dissected for post-mortem T2-weighted MRI (125 μm isotropic resolution, TR/TE: 1500/60.57 ms) and diffusion-weighted MRI (0.5 mm isotropic resolution, b-values=1800, 3400, and 5200 s/mm^2, with 30, 40, and 90 diffusion directions, respectively, and 6 A_0 images). Image data were acquired using a 9.4T/31cm horizontal-bore Bruker AV3 HD animal

scanner equipped with a high-performance 12-cm gradient set, capable of 660 mT/m maximum gradient strength, and a 72mm quadrature birdcage RF coil. Diffusion tensor estimation and tractography were performed using DSI studio (http://dsi-studio.labsolver.org). The accuracy of b-table orientation was examined by comparing fiber orientations with those of a population-averaged template[80]. The restricted diffusion was quantified using restricted diffusion imaging[81]. The diffusion data were reconstructed using generalized q-sampling imaging[82] with a diffusion sampling length ratio of 0.6.

For fiber tracking to characterize the thalamocortical projections, we used a tracking threshold of 0, angular threshold of 0, and a step size of 1 mm. Tracks with lengths shorter than 20 mm or longer than 200 mm were discarded. A total of 10,000 tracks were placed. Topology informed pruning[83] was applied to the tractography with 2 interactions to remove false connections. We selected each of three regions of the monkey motor-sensory thalamus (the ventral anterolateral region (VAL), ventral laterolateral region (VLL), and ventral posterolateral region (VPL)) as a seed to create tracks that projected to the cortical areas of interest: the primary somatosensory cortex (S1), the primary motor cortex (M1), the dorsal premotor cortex (PMd), and the supplementary motor area (SMA). Cortical and subcortical regions were mapped using the built-in primate CVIM atlas[84] and confirmed by certified neurosurgeons (Dr. Jorge Gonzalez-Martinez). We then calculated the volume of the tracts that projected from each motor thalamic region to each cortical region. We then normalized the volume of each tract by the total volume of projections from all motor thalamic regions to all cortical regions.

To analyze the selectivity of projections to only M1 from each of the motor-sensory thalamus nuclei, we computed a receiver operating characteristic (ROC) curve comparing the true positive rate and false positive rate of projections to M1 compared to those not to M1. We counted both rates while thresholding at each unique normalized volume. We then computed the area under the ROC curve for the VPL, VLL, and VAL.

To quantify the projections from the area of stimulation of the VLL DBS electrode, we manually drew a region, based on the size of the VLL thermal-ablation lesion. We then mirrored this region to the intact contralateral side (due to disruption of thalamocortical fibers by the lesion) and selected it as the seed. S1, M1, PMd, and SMA were selected as regions of interest. We used the same tracking parameters as above. We then calculated the volume of each tract normalized by the total volume of tracts from the area of stimulation to all cortical areas.

To quantify the damaged cortico-spinal tract (CST), we used a tracking threshold of 0, angular threshold of 0, and a step size of 0 mm. Tracks with lengths shorter than 30 mm or longer than 500 mm were discarded. A total of 10,000 tracks were placed. Topology informed pruning was applied to the tractography with 2 interactions to remove false connections. To reconstruct the CST, we manually drew seed regions in the left and right cerebral peduncles (confirmed by neurosurgeon, Dr. Jorge Gonzalez-Martinez) and the respective left and right motor cortices as regions of interest. We then calculated the volume of each CST and normalized it by the combined volume of the left and right CST.

Analysis of cortical activity

The broadband cortical data was first bandpass filtered between 10 and 5000 Hz with a 3rd order Butterworth filter and 1ms blanking was applied over stimulation artifacts. We then extracted a 25 ms window (5ms before stimulation, 20ms after stimulation) to capture the entirety of the cortical evoked potential. We then calculated the peak to peak amplitude and averaged it across all stimulation trials. We quantified multi-unit activity offline by calculating the average spike count across all trials for each channel. Cortical spikes were detected with a threshold of 3-3.5 (MK-SC: 3, MK-SZ: 3, MK-OP: 3.5, MK-HS: 3, MK-JC: 3) standard deviations above baseline for each channel of the 2 Utah arrays. The average spike counts were baseline corrected and were calculated using a bin size of 2 ms. We blanked 13 ms after stimulation to remove stimulation artifacts.

To analyze antidromic potentials to IC stimulation, we recorded local field potentials in the M1 Utah array when stimulating the IC at 2 Hz. We then sent a 100 ms 100 Hz burst of stimulation to the VLL preceding a single pulse of IC stimulation at various delays (2 ms, 5 ms, 10 ms, 50 ms). We applied the same filtering to the cortical data as above. We extracted a 45 ms window (5ms before IC stimulation, 40 ms after IC stimulation) to capture the entire antidromic potential. We then calculated the peak to peak amplitude of the antidromic potential and averaged it across all stimulation trials.

To calculate the frequency dependent cortical responses to VLL, we took the bandpass filtered cortical evoked potentials over M1 and extracted 12 ms windows (2 ms before stimulation, 10 ms after stimulation) for each stimulation pulse at a variety of VLL frequencies (VLL stim 10, 50, 80, and 100 Hz). We then calculated the peak to peak amplitude of the evoked potential over the time range of 1.5 to 10 ms after the simulations and averaged it across all stimulation trials.

Analysis of muscle activity and kinematics

Electromyographic activity was bandpass filtered between 30 and 800 Hz with a 3rd order Butterworth filter. We then computed the stimulation triggered averages (window from 5 ms to 25 ms after IC stimulation) of motor evoked potentials and calculated the peak to peak amplitude for each pulse of IC stimulation and each muscle.

Kinematics were recorded by a GoPro® Camera and analyzed through Deeplabcut[85], a neural network for 2D and 3D markerless pose estimation based on transfer learning. A subset of video frames (40-80 frames) per condition were selected by Deeplabcut to capture diversity of the movement. Next, we manually labeled the thumb, index finger, wrist, and elbow in each of those frames. With the labeled frames, we used Deeplabcut to create a training network by merging all extracted labeled frames. We then used the trained network to analyze all the videos and extract the kinematic traces for each of the labeled body points. We calculated the peak to peak amplitude in pixels of each joint for each pulse of IC stimulation.

Analysis of frequency dependent modulation of muscle responses

For each animal, muscle, and IC paired VLL stimulation (10, 50, 80, 100, and 200 Hz) protocol we concatenated all MEP responses from each IC stimulation pulse (window from 0 ms to 25 ms after IC stimulation). We then visually inspected and characterized these MEP traces according

to five criteria[43]: 1) “no potentiation” - the responses are consistent with IC alone stimulation, 2) “initial adaptation” - the responses at the start of the stimulation train are variable and then become potentiated, 3) “potentiation” - the responses are increased as compared to IC alone, 4) “attenuation” - the responses decrease through time, 5) “suppression” - the responses are suppressed through time. In order to ensure that the classifications were not biased by the muscle type or stimulation protocol, the MEP traces were unlabeled and presented in a random order during the visual inspection. For each unique stimulation protocol, we calculated its probability distribution over all muscles and animals.

Analysis of spinal activity

We applied the same filtering and extraction process to the spinal evoked potentials as we did to the cortical evoked potentials (filter 10-5000 Hz 3rd order Butterworth and 25 ms windows). To identify the antidromic response from the VLL stimulation, we calculated the peak to peak amplitude and response onset within the first 5 ms following VLL stimulation across all channels of the intraspinal probe. Using the intraspinal probe map we were able to distinguish the ventral, intermediate, and dorsal areas on the probe. In order to compare the responses across animals, we normalized the peak to peak amplitude by the maximum value for each animal independently.

When assessing the frequency dependent effects of VLL stimulation paired with IC stimulation on the spinal responses, we blanked the IC stimulation artifact between 250 us before stimulation and 500 us after the stimulation pulse ended. We then calculated the area under the curve (AUC) of the spinal evoked potentials for each VLL stimulation protocol (10, 50, 80, and 100Hz). The AUC were calculated from 5 to 10 ms after IC stimulation to exclude any stimulation artifacts and secondary post-synaptic responses. The AUC were compared against the AUC of the spinal responses from IC stimulation alone for potentiation or attenuation.

Human participants

We performed electrophysiological experiments on n=4 human subjects (2 males and 2 females) of age 69.5 ± 8.54 (mean±std) who presented with medically-intractable asymmetric Essential Tremor (ET) symptoms and were undergoing DBS implantation of the VIM/VOP nucleus (ventralis intermediate nucleus/ventralis oralis posterior), which corresponds to the VLL nucleus in monkeys. Experiments were performed from March 2022 to August 2022. We tested the least symptomatic arm to better approximate normal function. Additionally, we tested a traumatic brain injury (TBI01) patient (male in his 40’s) who had suffered subarachnoid hemorrhaging from a motor vehicle accident. This hemorrhage led to multiple foci of traumatic infarcts in both frontal lobes (**Figure 8a**, more pronounced in the left than the right hemisphere) and evidence of diffuse axonal injury involving the CST and bilateral edema of the cerebral peduncles and pons. Consequently, TBI01 suffered from hemiparesis of the right side and left upper extremity muscle weakness and tremor. The patient was recommended for bilateral DBS electrode implant to treat the post-traumatic tremor. The DBS implantation surgery and intra-operative experiment occurred in April 2022. The behavioral force tasks were collected in September and October of 2022. All intra-operative procedures were approved by the University of Pittsburgh Institutional Review Board (STUDY21040121). The behavioral experiments were approved by the University of Pittsburgh Institutional Review Board (STUDY21100020).

Human intraoperative data acquisition and electrophysiology

Pairs of needle electrodes (Rhythmlink) were implanted subcutaneously in the deltoid, biceps brachii, triceps brachii, flexors (flexor carpi ulnaris), extensor (extensor carpi radialis longus), and abductor pollicis brevis (APB) to record MEPs. Prior to DBS insertion, a subdural strip electrode (6 contact platinum subdural electrode, AD-TECH Medical Instrument Corporation, Oak Creek, WI) was implanted over the cortical surface with verification of positioning provided using median nerve somatosensory evoked potential (SSEP) phase reversal (PR) mapping to locate the hand representation of S1 cortex and the approximate location of the central sulcus[46]. The electrode position was adjusted using direct cortical stimulation (DCS) and recording of DCS MEPs to contralateral upper extremity muscles. We located the contact over the precentral gyrus that generated the largest amplitude MEP in the hand muscle (APB). DCS of the hand representation of M1 was provided using trains of 5 stimulation pulses (0.5 ms) at 400 Hz every two seconds at amplitudes up to 15mA using an intraoperative neurophysiological monitoring system (XLTEK Protektor, Natus Medical). Detailed information on the stimulation parameters used for DCS for each subject are reported in **Supplementary Table 4.** After implantation of the subdural strip electrode, the surgery continued following standard clinical procedures and DBS electrodes were implanted in the VIM/VOP nucleus bilaterally using subcortical mapping techniques. The electrophysiology experiments were performed following completion of the clinical procedure, with the subject maintained under anesthesia with propofol. Specifically, DCS MEPs from stimulation of the optimal electrode contact over the hand representation of the primary motor cortex were recorded without and with continuous stimulation of the VIM/VOP nucleus (DBS contacts -1 +8) at 50, 80, and 100Hz with pulses of 100us and amplitude of 3mA. MEPs were collected for 100 ms trials following each DCS stimulation burst and recorded using the XLTEK system at a sampling frequency of 6000 Hz. Stimulation of the VIM/VOP was delivered via the Boston Scientific clinician programmer that connects via Bluetooth to an external trial stimulator. The same DBS electrode was used to generate cortical evoked potentials in the subdural strip electrode that were recorded using the Ripple Neuro Grapevine and Trellis software at a sampling frequency of 30000 Hz.

Behavioral experimental recordings and analysis

To measure the level of voluntary force control, the participant was asked to grasp a force dynamometer (Pinch/Grip Digital Myometer, MIE Medical Research, Yorkshire, UK), which recorded the force in newtons at a sampling rate of 30000 Hz. We prepared a task where the participant modulated their force between two limits (55-70% of maximum voluntary contraction measured with DBS OFF). A screen provided feedback of the target force and the participant's applied force. We calculated the root-mean-squared error between the applied force and the expected force at each time point.

To calculate the frequency power of the force trace, we filtered with a band-pass 2nd order Butterworth filter (cut-off frequencies of 2-5000 Hz) and performed a fast fourier transform of the hold portion of the force task. We then compared the average power from 6-12 Hz (frequency range of Essential Tremor) during VIM/VOP stimulation on and off.

Analysis of intraoperative cortical and muscle activity

Electrocorticographic data were filtered with a band-pass 2nd order Butterworth filter (cut-off frequencies 10-500 Hz) and a 60 Hz notch 2nd order Butterworth filter. The stimulation artifact was blanked. We extracted epochs of 30 ms (10 ms before and 20 ms after the stimulus onset) and computed stimulation triggered averages. We calculated the peak to peak amplitude of each cortical evoked potential as the difference between the maximum and minimum voltage value in the interval 3-15 ms following the stimulus onset.

To quantify DCS MEPs recorded from triggered electromyographic activity, we computed the stimulation triggered averages (EMG from 10 ms to 75 ms after stimulation) and calculated the AUC for each muscle.

Human HDFT, Volume of Activation, and Lesion Segmentation

HDFT

The diffusion images were acquired on a SIEMENS Prisma Fit scanner using a diffusion sequence (2mm isotropic resolution, TE/TR= 99.2 ms/2490 ms, 257 diffusion sampling with maximum b-value 4010 s/mm²). The accuracy of b-table orientation was examined by comparing fiber orientations with those of a population-averaged template[80]. The tensor metrics were calculated using DWI with b-value lower than 1750 s/mm².

For fiber tracking, we used a tracking threshold of 0, angular threshold of 50, and a step size of 1 mm. Tracks with lengths shorter than 30 mm or longer than 500 mm were discarded. A total of 10,000 tracks were placed. Topology informed pruning was applied to the tractography with 2 interactions to remove false connections. To quantify the projections from the area of stimulation of the VIM/VOP DBS electrode, we manually drew a region at the stimulation contact and considered it as the seed region. S1, M1, PMd and SMA were the regions of interest. We then calculated the volume of each tract normalized by the total volume of tracts from the area of stimulation to all cortical areas.

Volume of Activation

After DBS implantation of the VIM/VOP DBS electrode, patients underwent post-implant CT imaging (1.25 mm isotropic, GE Medical Systems) to reconstruct the DBS leads. With the reconstructed DBS leads, we modeled the volume of tissue activation (VTA) in each patient using the DBS analysis module inside BrainLab Quentry®. Specifically, we visualized a 3D reconstruction of VIM, DBS electrode, and the simulated VTAs from the anode and cathode of the DBS leads. We then aggregated the VTA from the non-TBI DBS patients (excluding TB01) and overlaid them on axial and coronal T2-weighted MRI images (1.6 mm isotropic, TR/TE = 9690/91 ms, 3T Siemens Prisma Fit).

Lesion Segmentation

In TB01, we highlighted areas of lesion caused by traumatic brain injury. Lesion segmentation was performed by board-certified neurosurgeon (Dr. Jorge Gonzalez-Martinez) from axial T2-flair images acquired by a 3T Siemens Prisma Fit Scanner (1.6 mm isotropic, TR/TE = 9690/91 ms).

Statistical Procedures

All statistical comparisons of means presented in this manuscript were performed using the bootstrap method, a non-parametric approach which makes no distributional assumptions on the observed data. Instead, bootstrapping uses resampling to construct empirical confidence intervals for quantities of interest. For each comparison, we construct bootstrap samples by drawing a sample with replacement from observed measurements, while preserving the number of measurements in each condition. We construct 10,000 bootstrap samples and, for each, calculate the difference in means of the resampled data. We employed one or two tailed bootstrapping with alphas of 0.05 (95% confidence interval), 0.01 (99% confidence interval), or 0.001 (99.9% confidence interval). The null hypothesis of no difference in the mean was rejected if 0 was not included in the confidence interval of the corresponding alpha value. If more than one comparison was being performed at once, we used a Bonferroni correction by dividing the alpha value by the number of pairwise comparisons being performed.

SUPPLEMENTARY TABLES:

Animal ID	Species	Sex	Age (Yr)	Weight	Experiments
MK-SC	Macaca Fascicularis	M	4	5.4 kg	Cortical Evoked Potentials/Spike Counts
MK-SZ	Macaca Fascicularis	M	4	5.9 kg	Cortical Spike Counts Kinematic Recording (pre/post lesion)
MK-OP	Macaca Fascicularis	F	6	6 kg	Cortical Evoked Potentials Antidromic Potentials EMG Recordings (pre/post lesion) Kinematic Recording (pre/post lesion) Radial Nerve Control Frequency Analysis
MK-HS	Macaca Mulatta	M	7	12 kg	Cortical Evoked Potentials/Spike Counts Antidromic Potentials EMG Recordings (pre/post lesion) Kinematic Recording (pre/post lesion) Radial Nerve Control Frequency Analysis
MK-JC	Macaca Fascicularis	M	6	8.2kg	Cortical Evoked Potentials Antidromic Potentials EMG Recordings (pre/post lesion) Kinematic Recording (pre/post lesion) Radial Nerve Control Frequency Analysis Force Measurements (pre/post lesion)

Supplementary Table 1: Summary of monkey demographic and experiments performed.

Animal ID	IC Stimulation Parameters (Amplitude, Pulse Width)	VLL Stimulation Parameters (Amplitude, Pulse Width)	VLL Burst Parameters (Amplitude, Pulse Width)	Radial Nerve Stimulation Parameters (Amplitude, Pulse Width)
MK-SC	–	4.8 mA, 2 ms	–	–
MK-SZ	800 µA, 800 µs	1 mA, 2 ms	–	–
MK-OP	2 mA, 3ms	1.5 mA, 100 µs	1 mA, 100 µs	120 µA, 100 µs
MK-HS	1 mA, 1 ms	2 mA, 300 µs	2 mA, 300 µs	90 µA, 100 µs
MK-JC	2 mA, 1 ms	2 mA, 300 µs	2 mA, 300 µs	105 µA, 100 µs

Supplementary Table 2: Simulation parameters for IC, VLL, and radial nerve. – means that that stimulation was not performed in that particular animal

Animal ID	Temperature	Time
MK-SC	90℃	60 seconds
MK-SZ	75℃	60 seconds
MK-OP	80℃	60 seconds
MK-HS	80℃	60 seconds
MK-JC	80℃	30 seconds

Supplementary Table 3: Temperature and time used to create a lesion of the CST within the internal capsule.

Subject	DCS amplitude	VIM/VOP frequency
S01	8 mA, 9 mA, 10 mA	50 Hz, 100 Hz
S02	13 mA, 14 mA, 15 mA	50 Hz, 80 Hz
S03	7 mA, 11 mA	50 Hz, 80 Hz, 100 Hz
S04	8 mA, 10 mA, 12 mA	50 Hz, 80 Hz, 100 Hz

Supplementary Table 4: Stimulation parameters for DCS and VIM/VOP in humans. The amplitude of stimulation of the VIM/VOP was always at 3mA and within contact -1 and +8.

REFERENCES

1. Prabhakaran, S. *et al.* Inter-individual variability in the capacity for motor recovery after ischemic stroke. *Neurorehabilitation and neural repair* **22**, 64–71 (2008).
2. Zhu, L. L., Lindenberg, R., Alexander, M. P. & Schlaug, G. Lesion load of the corticospinal tract predicts motor impairment in chronic stroke. *Stroke* **41**, 910–915 (2010).
3. Maraka, S. *et al.* Degree of corticospinal tract damage correlates with motor function after stroke. *Annals of clinical and translational neurology* **1**, 891–899 (2014).
4. Lin, D. J. *et al.* Corticospinal tract injury estimated from acute stroke imaging predicts upper extremity motor recovery after stroke. *Stroke* **50**, 3569–3577 (2019).
5. Skolarus, L., Meurer, W., Burke, J., Bettger, J. P. & Lisabeth, L. Effect of insurance status on postacute care among working age stroke survivors. *Neurology* **78**, 1590–1595 (2012).
6. Zaloshnja, E., Miller, T., Langlois, J. A. & Selassie, A. W. Prevalence of long-term disability from traumatic brain injury in the civilian population of the United States, 2005. *The Journal of head trauma rehabilitation* **23**, 394–400 (2008).
7. Pollock, A. *et al.* Physical rehabilitation approaches for the recovery of function and mobility following stroke. *Cochrane Database of Systematic Reviews* (2014).
8. Pollock, A. *et al.* Interventions for improving upper limb function after stroke. *Cochrane Database of Systematic Reviews* (2014).
9. Krakauer, J. W. & Carmichael, S. T. *Broken movement: the neurobiology of motor recovery after stroke*. (MIT Press, 2017).
10. Hammerbeck, U. *et al.* The strength of the corticospinal tract not the reticulospinal tract determines upper-limb impairment level and capacity for skill-acquisition in the sub-acute post-stroke period. *Neurorehabilitation and neural repair* **35**, 812–822 (2021).
11. Rosso, C. *et al.* Contribution of corticospinal tract and functional connectivity in hand motor impairment after stroke. *PloS one* **8**, e73164 (2013).

12. Clayton, E., Kinley-Cooper, S., Weber, R. & Adkins, D. Brain stimulation: Neuromodulation as a potential treatment for motor recovery following traumatic brain injury. *Brain research* **1640**, 130–138 (2016).

13. Simonetta-Moreau, M. Non-invasive brain stimulation (NIBS) and motor recovery after stroke. *Annals of physical and rehabilitation medicine* **57**, 530–542 (2014).

14. Lozano, A. M. *et al.* Deep brain stimulation: current challenges and future directions. *Nature Reviews Neurology* **15**, 148–160 (2019).

15. Krauss, J. K. *et al.* Technology of deep brain stimulation: current status and future directions. *Nature Reviews Neurology* **17**, 75–87 (2021).

16. Ni, Z., Udupa, K., Hallett, M. & Chen, R. Effects of deep brain stimulation on the primary motor cortex: insights from transcranial magnetic stimulation studies. *Clinical Neurophysiology* **130**, 558–567 (2019).

17. Kibleur, A. & David, O. Electroencephalographic read-outs of the modulation of cortical network activity by deep brain stimulation. *Bioelectronic medicine* **4**, 1–9 (2018).

18. Dale, J., Schmidt, S. L., Mitchell, K., Turner, D. A. & Grill, W. M. Evoked potentials generated by deep brain stimulation for Parkinson's disease. *Brain stimulation* (2022).

19. Kuriakose, R. *et al.* The nature and time course of cortical activation following subthalamic stimulation in Parkinson's disease. *Cerebral cortex* **20**, 1926–1936 (2010).

20. Molnar, G. *et al.* Changes in cortical excitability with thalamic deep brain stimulation. *Neurology* **64**, 1913–1919 (2005).

21. Ni, Z. *et al.* Pallidal deep brain stimulation modulates cortical excitability and plasticity. *Annals of neurology* **83**, 352–362 (2018).

22. Hooks, B. M. *et al.* Organization of cortical and thalamic input to pyramidal neurons in mouse motor cortex. *Journal of Neuroscience* **33**, 748–760 (2013).

23. Rouiller, E. M., Tanne, J., Moret, V. & Boussaoud, D. Origin of thalamic inputs to the primary, premotor, and supplementary motor cortical areas and to area 46 in macaque

monkeys: a multiple retrograde tracing study. *Journal of Comparative Neurology* **409**, 131–152 (1999).

24. Holsapple, J. W., Preston, J. B. & Strick, P. L. The origin of thalamic inputs to the" hand" representation in the primary motor cortex. *Journal of Neuroscience* **11**, 2644–2654 (1991).

25. Strick, P. L. Multiple sources of thalamic input to the primate motor cortex. *Brain research* **88**, 372–377 (1975).

26. Goldberg, M. E. The neurology clinic needs monkey research. *Proceedings of the National Academy of Sciences* **116**, 26255–26258 (2019).

27. Courtine, G. *et al.* Can experiments in nonhuman primates expedite the translation of treatments for spinal cord injury in humans? *Nature medicine* **13**, 561–566 (2007).

28. Lemon, R. N. Descending pathways in motor control. *Annu. Rev. Neurosci.* **31**, 195–218 (2008).

29. Paek, S. B. *et al.* Frequency-dependent functional neuromodulatory effects on the motor network by ventral lateral thalamic deep brain stimulation in swine. *Neuroimage* **105**, 181–188 (2015).

30. Hassler, R. Anatomy of the thalamus. *Archiv fur Psychiatrie und Nervenkrankheiten, vereinigt mit Zeitschrift fur die gesamte Neurologie und Psychiatrie* **184**, 249–256 (1950).

31. Shaltenbrand, G. Introduction to Stereotaxis with an Atlas of the Human Brain. *Stuttgart* (1959).

32. Nambu, A., Yoshida, S. & Jinnai, K. Projection on the motor cortex of thalamic neurons with pallidal input in the monkey. *Experimental brain research* **71**, 658–662 (1988).

33. Krack, P. *et al.* Surgery of the motor thalamus: problems with the present nomenclatures. *Movement disorders: official journal of the Movement Disorder Society* **17**, S2–S8 (2002).

34. Fang, P.-C., Stepniewska, I. & Kaas, J. H. The thalamic connections of motor, premotor, and prefrontal areas of cortex in a prosimian primate (Otolemur garnetti). *Neuroscience* **143**, 987–1020 (2006).

35. Zhu, G. *et al.* The accuracy and feasibility of robotic assisted lead implantation in nonhuman primates. *Neuromodulation: Technology at the Neural Interface* **22**, 441–450 (2019).

36. Ho, J. *et al.* Robot Assisted Neurosurgery for High-Accuracy, Minimally-Invasive Deep Brain Electrophysiology in Monkeys,. in *IEEE Proceedings IEEE Engineering in Medicine & Biology Society (EMBC)* (IEEE, 2022).

37. Xu, F. *et al.* Improved accuracy using a modified registration method of ROSA in deep brain stimulation surgery. *Neurosurgical Focus* **45**, E18 (2018).

38. Kuramoto, E. *et al.* Two types of thalamocortical projections from the motor thalamic nuclei of the rat: a single neuron-tracing study using viral vectors. *Cerebral cortex* **19**, 2065–2077 (2009).

39. Salt, T., Meier, C., Seno, N., Krucker, T. & Herrling, P. Thalamocortical and corticocortical excitatory postsynaptic potentials mediated by excitatory amino acid receptors in the cat motor cortexin vivo. *Neuroscience* **64**, 433–442 (1995).

40. Liew, Y. J. *et al.* Inferring thalamocortical monosynaptic connectivity in vivo. *Journal of Neurophysiology* **125**, 2408–2431 (2021).

41. Rudomin, P. & Schmidt, R. F. Presynaptic inhibition in the vertebrate spinal cord revisited. *Experimental brain research* **129**, 1–37 (1999).

42. Sharma, M. *et al.* Novel Evoked Synaptic Activity Potentials (ESAPs) elicited by Spinal Cord Stimulation. *bioRxiv* 2023–02 (2023).

43. Greiner, N. *et al.* Recruitment of upper-limb motoneurons with epidural electrical stimulation of the cervical spinal cord. *Nature Communications* **12**, 435 (2021).

44. Volkmann, J., Herzog, J., Kopper, F. & Deuschl, G. Introduction to the programming of deep brain stimulators. *Movement disorders: official journal of the Movement Disorder Society* **17**, S181–S187 (2002).

45. Vinas, F. *et al.* In vivo and in vitro study of the lesions produced with a computerized radiofrequency system. *Stereotactic and functional neurosurgery* **58**, 121–133 (1992).

46. Cedzich, C., Taniguchi, M., Schäfer, S. & Schramm, J. Somatosensory evoked potential phase reversal and direct motor cortex stimulation during surgery in and around the central region. *Neurosurgery* **38**, 962–970 (1996).

47. Agarwal, S. & Biagioni, M. C. Essential tremor. (2018).

48. Lozano, A. M. & Lipsman, N. Probing and regulating dysfunctional circuits using deep brain stimulation. *Neuron* **77**, 406–424 (2013).

49. Bucher, D. & Goaillard, J.-M. Beyond faithful conduction: short-term dynamics, neuromodulation, and long-term regulation of spike propagation in the axon. *Progress in neurobiology* **94**, 307–346 (2011).

50. Llinás, R. R., Leznik, E. & Urbano, F. J. Temporal binding via cortical coincidence detection of specific and nonspecific thalamocortical inputs: a voltage-dependent dye-imaging study in mouse brain slices. *Proceedings of the National Academy of Sciences* **99**, 449–454 (2002).

51. Miocinovic, S. *et al.* Computational analysis of subthalamic nucleus and lenticular fasciculus activation during therapeutic deep brain stimulation. *Journal of neurophysiology* **96**, 1569–1580 (2006).

52. Rosenbaum, R. *et al.* Axonal and synaptic failure suppress the transfer of firing rate oscillations, synchrony and information during high frequency deep brain stimulation. *Neurobiology of disease* **62**, 86–99 (2014).

53. Ashkan, K., Rogers, P., Bergman, H. & Ughratdar, I. Insights into the mechanisms of deep brain stimulation. *Nature Reviews Neurology* **13**, 548–554 (2017).

54. Elias, G. J., Namasivayam, A. A. & Lozano, A. M. Deep brain stimulation for stroke: Current uses and future directions. *Brain stimulation* **11**, 3–28 (2018).

55. Cooper, I., Upton, A. & Amin, I. Reversibility of chronic neurologic deficits. Some effects of electrical stimulation of the thalamus and internal capsule in man. *Stereotactic and Functional Neurosurgery* **43**, 244–258 (1980).

56. Phillips, N. & Bhakta, B. Affect of deep brain stimulation on limb paresis after stroke. *The Lancet* **356**, 222–223 (2000).

57. Franzini, A., Cordella, R., Nazzi, V. & Broggi, G. Long-term Chronic stimulation of internal capsule in poststroke pain and Spasticity. *Stereotactic and functional neurosurgery* **86**, 179–183 (2008).

58. Cooperrider, J. *et al.* Chronic deep cerebellar stimulation promotes long-term potentiation, microstructural plasticity, and reorganization of perilesional cortical representation in a rodent model. *Journal of Neuroscience* **34**, 9040–9050 (2014).

59. Pirondini, E. *et al.* Poststroke arm and hand paresis: should we target the cervical spinal cord? *Trends in neurosciences* (2022).

60. Owen, R. L. *et al.* Effectiveness of Thalamic Ventralis Oralis Anterior and Posterior Nuclei Deep Brain Stimulation for Posttraumatic Dystonia. *Mayo Clinic Proceedings: Innovations, Quality & Outcomes* **6**, 137–142 (2022).

61. Hummel, F. C. & Cohen, L. G. Non-invasive brain stimulation: a new strategy to improve neurorehabilitation after stroke? *The Lancet Neurology* **5**, 708–712 (2006).

62. Hummel, F. C. *et al.* Controversy: Noninvasive and invasive cortical stimulation show efficacy in treating stroke patients. *Brain stimulation* **1**, 370–82 (2008).

63. Coscia, M. *et al.* Neurotechnology-aided interventions for upper limb motor rehabilitation in severe chronic stroke. *Brain : a journal of neurology* **142**, 2182–2197 (2019).

64. Nitsche, M. A. & Paulus, W. Excitability changes induced in the human motor cortex by weak transcranial direct current stimulation. *The Journal of physiology* **527**, 633 (2000).

65. Triccas, L. T. *et al.* Multiple sessions of transcranial direct current stimulation and upper extremity rehabilitation in stroke: a review and meta-analysis. *Clinical Neurophysiology* **127**, 946–955 (2016).

66. Lefaucheur, J. P. *et al.* Evidence-based guidelines on the therapeutic use of repetitive transcranial magnetic stimulation (rTMS). *Clinical neurophysiology : official journal of the International Federation of Clinical Neurophysiology* **125**, 2150–2206 (2014).

67. Lefaucheur, J. P. *et al.* Evidence-based guidelines on the therapeutic use of transcranial direct current stimulation (tDCS). *Clinical neurophysiology : official journal of the International Federation of Clinical Neurophysiology* **128**, 56–92 (2017).

68. Plow, E. B. & Machado, A. Invasive neurostimulation in stroke rehabilitation. *Neurotherapeutics* **11**, 572–582 (2014).

69. Bahr-Hosseini, M. *et al.* Transcranial Electrical Stimulation in Stroke EaRly After onset Clinical Trial (TESSERACT). *Brain Stimulation: Basic, Translational, and Clinical Research in Neuromodulation* **16**, 236 (2023).

70. Triccas, L. T. *et al.* A double-blinded randomised controlled trial exploring the effect of anodal transcranial direct current stimulation and uni-lateral robot therapy for the impaired upper limb in sub-acute and chronic stroke. *NeuroRehabilitation* **37**, 181–191 (2015).

71. Triccas, L. T. *et al.* A mixed-methods study exploring the combination of non-invasive brain stimulation and robot therapy for the impaired upper limb in stroke. *Physiotherapy* **101**, e1496–e1497 (2015).

72. Ang, K. K. *et al.* Facilitating effects of transcranial direct current stimulation on motor imagery brain-computer interface with robotic feedback for stroke rehabilitation. *Archives of physical medicine and rehabilitation* **96**, S79–S87 (2015).

73. Di Lazzaro, V. *et al.* Combining robotic training and non-invasive brain stimulation in severe upper limb-impaired chronic stroke patients. *Frontiers in neuroscience* **10**, 88 (2016).

74. Straudi, S. *et al.* tDCS and robotics on upper limb stroke rehabilitation: effect modification by stroke duration and type of stroke. *BioMed research international* **2016**, (2016).

75. Simonetti, D. *et al.* Literature review on the effects of tDCS coupled with robotic therapy in post stroke upper limb rehabilitation. *Frontiers in human neuroscience* **11**, 268 (2017).

76. Fenoy, A. J. & Simpson, R. K. Risks of common complications in deep brain stimulation surgery: management and avoidance. *Journal of neurosurgery* **120**, 132–139 (2014).

77. Sharma, D. & Vavilala, M. S. Perioperative management of adult traumatic brain injury. *Anesthesiology clinics* **30**, 333–346 (2012).

78. Mehdi, Z., Birns, J., Partridge, J., Bhalla, A. & Dhesi, J. Perioperative management of adult patients with a history of stroke or transient ischaemic attack undergoing elective non-cardiac surgery. *Clinical medicine* **16**, 535 (2016).

79. Dawson, J. *et al.* Vagus nerve stimulation paired with rehabilitation for upper limb motor function after ischaemic stroke (VNS-REHAB): a randomised, blinded, pivotal, device trial. *The Lancet* **397**, 1545–1553 (2021).

80. Yeh, F. C. *et al.* Population-averaged atlas of the macroscale human structural connectome and its network topology. *NeuroImage* **178**, 57–68 (2018).

81. Yeh, F., Liu, L., Hitchens, T. K. & Wu, Y. L. Mapping immune cell infiltration using restricted diffusion MRI. *Magnetic resonance in medicine* **77**, 603–612 (2017).

82. Yeh, F.-C., Wedeen, V. J. & Tseng, W.-Y. I. Generalized ${q} $-sampling imaging. *IEEE transactions on medical imaging* **29**, 1626–1635 (2010).

83. Yeh, F.-C. *et al.* Automatic removal of false connections in diffusion MRI tractography using topology-informed pruning (TIP). *Neurotherapeutics* **16**, 52–58 (2019).

84. Calabrese, E. *et al.* A diffusion tensor MRI atlas of the postmortem rhesus macaque brain. *Neuroimage* **117**, 408–416 (2015).

85. Mathis, A. *et al.* DeepLabCut: markerless pose estimation of user-defined body parts with deep learning. *Nature neuroscience* **21**, 1281–1289 (2018).